A xenon collisional-radiative model applicable to electric propulsion devices: III. Determination of the ionization fraction in low-temperature xenon plasma by using ionic and atomic 6p lines

Xi-Ming Zhu^{1,2,*}, Yan-Fei Wang^{1,*}, Sheng-Feng Meng¹, Yang Wang¹, Zhong-Xi Ning^{1,2,*}, Da-Ren Yu^{1,2} and Klaus Bartschat^{3,*}

E-mail: simon.ximing.zhu@outlook.com, arvin.yanfei.wang@outlook.com, ningzx@hit.edu.cn and klaus.bartschat@drake.edu

1

Received 24 November 2022, revised 7 September 2023 Accepted for publication 19 September 2023 Published 29 September 2023



Abstract

The ionization fraction is a key figure of merit for optimizing the performance of plasma device. This work presents an optical emission spectroscopy (OES) method to determine the ionization fraction in low-temperature xenon plasma. The emission line-ratio of xenon ionic and atomic 6p-6s transitions is used in this method. A comprehensive collisional-radiative model developed in our previous work is employed to describe the relationship between the line-ratios and the plasma parameters. It is found that some special line-ratios have a sensitive relationship to the ionization fraction, e.g. the ratio of the 460.30 nm line and 828.01 nm lines. These line-ratios are selected for the diagnostic method. The method is demonstrated in a magnetized discharge chamber. The axially-resolved emission spectra of the ionization chamber are measured, and from those the ionization fraction along the chamber axis is determined via the OES method. The axially-resolved ionization fraction is found to be dependent on the magnetic field and agrees well with those obtained from a Langmuir probe. In the experiment, the probe is overheated under some conditions, possibly due to the bombardment by energetic particles. In this case, no results can be obtained from the probe, while the OES method can still obtain reasonable results. Combined with optical tomography and spectral imaging technology, the OES method can also provide the spatial distribution of the ionization fraction, which is needed for revealing the discharge mechanisms of plasma devices.

1361-6595/23/095019+20\$33.00 Printed in the UK

¹ Harbin Institute of Technology, Harbin, Heilongjiang 150001, People's Republic of China

² Key Laboratory of Aerospace Plasma Propulsion, Ministry of Industry and Information Technology, Harbin, Heilongjiang 150001, People's Republic of China

³ Department of Physics and Astronomy, Drake University, Des Moines, IA 50311, United States of America

^{*} Authors to whom any correspondence should be addressed.

Keywords: optical emission spectroscopy, ionization fraction, line-ratio method, magnetized discharge chamber, electric propulsion

(Some figures may appear in colour only in the online journal)

1. Introduction

Low-temperature plasma device is one of the key equipment in functional material producing, material processing, and semiconductor manufacturing [1–8]. Plasma devices applying different types of discharge is developed for these scenarios, e.g. inductively coupled plasma type [9, 10], electron cyclotron resonance (ECR) type [11, 12], and magnetized DC type [13, 14]. The ionization fraction (x_e , defined as the ratio of ion density n_{ion} to atom density n_{atom} with equation (1)) is a key figure of merit for evaluating the performance of the plasma devices and an important parameter for revealing the physics behind the discharge phenomena [15–18]. In addition, the ionization fraction can be used to evaluate the operating state of plasma propulsion devices, which is important for some space missions [19–22].

$$x_{\rm e} = \frac{n_{\rm ion}}{n_{\rm atom}}. (1)$$

In some kinds of plasmas, the ionization fraction is obtained from the ion density measured by a Langmuir probe or through a laser-based method [23, 24]. Numerical simulations are also used to estimate the ionization fraction [25, 26]. As a non-invasive method, optical emission spectroscopy (OES) is widely applied in the diagnostics of the electron temperature [27–30], the electron density [31, 32], and the gas temperature [33, 34]. Combined with the spectral imaging method, OES can obtain sub-millimeter-level spatially-resolved distributions of the above-mentioned plasma parameters [35, 36]. The literature shows that the spectral lines of ionic and atomic species have been observed simultaneously in argon, krypton, xenon, and iodine plasmas [37-40], and the emission lineratios of the ionic and atomic species are related to the ionization fraction [41, 42]. However, rarely are there quantitative OES methods reported for determining the ionization fraction, mainly due to the absence of reliable collisional-radiative (CR) models (CRMs) for the ionic species.

In our previous works, the cross-section data is obtained employing a fully-relativistic Dirac B-spline R-matrix (BSR) method for electron-impact excitation of xenon ions [43]. A comprehensive CRM is developed based on the BSR cross sections concerning both atomic and ionic excited species of xenon plasma [44]. Recently, similar model is developed based on these two works that concerning the kinetic mechanisms of atomic and ionic levels, and are examined with different plasmas [45]. But so far, no quantitative diagnostic method has been proposed to determine ionization fraction.

This work develops a quantitative line-ratio method for determining ionization fraction by analyzing the kinetic mechanism of the ionic and atomic 6*p* species based on the comprehensive CRM developed in [44]. We demonstrate this method

with a magnetized discharge chamber. Axially-resolved emission spectra are measured in the cylindrical chamber, from which the ionization fraction is obtained using the OES method. The result is compared with that obtained by a Langmuir probe. The applicable scenario of this method is analyzed. Furthermore, a simplified formula is presented, which enables investigators to quickly obtain an estimate of the ionization fraction. In particular, we discuss the common characteristics of the emission line-ratios that have sensitive relationships to the ionization fraction by analyzing the quantum numbers of the energy levels. The possibility of extending this 'ionic-atomic line-ratio' method to other plasmas, e.g. argon, krypton, and iodine plasmas, is also discussed from the perspective of atomic physics.

This paper is organized as follows. Section 2 describes the OES method, including a brief retrospect of the CRM, a kinetic analysis of the ionic and atomic excited species, and a detailed description of selecting specific line-ratios to determine the ionization fraction. Section 3 introduces the experiment. Here the structure of the discharge chamber and the experimental setup are presented. Section 4 presents the results and discussions of the present work. The OES method is examined by comparing the results with that of a Langmuir probe. The relationship between the ionization fraction and the magnetic field is investigated. This section also includes a simplified scheme, which enables a fast estimate of the ionization fraction in particular devices. Finally, our conclusions are summarized in section 5.

2. Method

This section describes the method for determining the ionization fraction by using the 6p–6s spectral lines of Xe^+ and neutral xenon. Section 2.1 gives a brief retrospect of the comprehensive xenon CRM developed earlier [43, 44]. In section 2.2, we investigate the contributions from different processes in populating and de-populating the atomic and ionic excited states. Section 2.3 analyzes the characteristics of the line-ratios from different excited levels and presents the scheme for determining the ionization fraction using these line-ratios.

2.1. CRM

CRMs for xenon plasmas have been developed and used in diagnostics for many years [27, 28, 45, 46]. However, due to limitations in fundamental cross-section data, these CRMs focus on the atomic species; the ionic species were not studied in detail. In our previous works, a fully relativistic Dirac BSR

No.	Configuration	Term	J	E (eV)	λ (nm)
Xe-I-1	$5p^5(^2P^{\circ}_{3/2})$ 6p	² [5/2]	3	9.721	881.9
Xe-I-2	$5p^5(^2P^0_{3/2}) 6p$	² [5/2]	2	9.686	904.6, 992.3
Xe-I-3	$5p^5(^2P^{\circ}_{3/2}) 6p$	² [3/2]	2	9.821	823.2, 895.2
Xe-I-4	$5p^5(^2P^0_{3/2}) 6p$	² [3/2]	1	9.580	980.0
Xe-I-5	$5p^5(^2P^0_{3/2}) 6p$	² [1/2]	1	9.789	840.9, 916.3
Xe-I-6	$5p^5(^2P^0_{3/2}) 6p$	² [1/2]	0	9.933	828.0
Xe-I-7	$5p^5(^2P^0_{1/2})$ 6p	² [3/2]	2	11.055	834.7
Xe-I-8	$5p^5(^2P^0_{1/2})$ 6p	² [3/2]	1	10.958	820.6, 893.1
Xe-I-9	$5p^5(^2P^0_{1/2}) 6p$	² [1/2]	1	11.069	764.2, 826.7
Xe-I-10	$5p^5(^2P^0_{1/2}) 6p$	² [1/2]	0	11.141	788.7

Table 1. Atomic 6*p* levels studied in the present Xe CRM. 'E' refers to the level energy relative to the ground state while ' λ ' is the vacuum wavelength of the relatively strong emission lines of these levels observed in the experiment.

method [43, 44] was applied to calculate the cross-section data for electron collisions with the Xe⁺ ion [43].

A comprehensive CRM concerning the kinetics of both Xe and Xe⁺ was developed based on these data [44] and examined experimentally [44, 47]. The model mainly considers the kinetics of the $5p^56s$, $5p^56p$, and $5p^55d$ energy levels of xenon atoms and the $5p^46s$, $5p^46p$, and $5p^45d$ energy levels of xenon ions. Some of the atomic $5p^57s$, $5p^57p$, and $5p^56d$ levels are also included in the CRM. The two ionic $5s^25p^5$ levels with J = 3/2 and 1/2 are considered as separate levels (bound energy of which are $E_b = 0$ eV and 1.306 eV, respectively). And the ionic level with configuration of $5s5p^6$ is also included. All the energy levels included in the CRM are listed in the appendix. Tables 1 and 2 list the atomic and ionic 6p levels of the CRM and the strong emission lines emitted by these 6p levels.

Both electron-induced and ion-induced excitation and ion-ization processes are considered for these energy levels, along with radiation, radiation-trapping, and transport-induced quenching. Considering the processes above, the rate balance equation for excited level *i* is written as:

$$\sum_{j \neq i} R_{j \to i}^{\text{col}} + \sum_{j > i} R_{j \to i}^{\text{rad}} + \sum_{j < i} R_{j \to i}^{\text{abs}} = \sum_{j \neq i} R_{i \to j}^{\text{col}} + \sum_{j < i} R_{i \to j}^{\text{rad}} + \sum_{j > i} R_{i \to j}^{\text{rads}} + R_{i \to j}^{\text{trans}}.$$
(2)

Here R is the reaction rate, the subscript 'j' indicates an energy level different from level i; 'j > i' means that the energy of level j is higher than level i. 'col', 'rad', 'abs', and 'trans' refer to collision, radiation, absorption, and transport processes, respectively. R^{col} can be calculated from the cross section, the electron energy distribution function, the electron temperature, and the particle density; R^{rad} can be calculated from the Einstein coefficient; the reaction rate of radiation-trapping R^{abs} is calculated using an escape factor which considers the hyperfine line splitting induced by isotope effect, which is detailed in [48].

The transport process can play an important role for the kinetics of some long-lived particles, e.g. the atomic and ionic metastable particles. A bipolar diffusion model under magnetization [49, 50] is used to calculate the rate of transportinduced quenching R^{trans} for ionic states. For atomic states, R^{trans} is calculated from the radius of the discharge chamber. By solving the rate balance equation (2), the density of the atomic and ionic excited species, the emission line intensities, and the contributions from different kinetic processes can be obtained. This information is used in the subsequent investigation.

2.2. Kinetic mechanism of 6p levels

In this section, the comprehensive CRM is used to analyze the kinetic mechanism of ionic and atomic 6p excited states. The percentage contribution of each process is used to evaluate the importance of the process in populating and de-populating the excited states. For process k, its percentage contribution ξ_k is written as:

$$\xi_k = \frac{R_k}{\sum R_x} \times 100. \tag{3}$$

Here R_k is the rate of process k, which is calculated from the comprehensive CRM.

According to the comprehensive CRM, spontaneous radiation dominates the depopulation of both the atomic and ionic 6p states, while electron collision processes dominate the population of these states in the pressure range of 10^{-3} – 10^{0} Pa and the electron density range $10^9 - 10^{12}$ cm⁻³. Note that the threshold energies of the various electron collision processes are different. Thus, the electron-impact processes are further grouped accordingly into: (i) electron-induced excitation from the ground-state (equations (4) and (5) below, $E_a \sim 9$ – 14 eV), with the sum of the percentage contributions from this group denoted by ξ_{gs} ; (ii) electron-induced transitions between excited states (equations (6) and (7) below, $E_a < 8$ eV), with the sum of the percentage contribution from this group being $\xi_{\rm ms}$; (iii) electron-induced ionization–excitation from the atom (equation (8), $E_a > 20$ eV), with the sum of the percentage contribution ξ_{i-e} . We write these processes as:

$$e + Xe \rightarrow e + Xe^*;$$
 (4)

Table 2. Ionic 6p levels in the CRM and their relatively strong emission lines. E is the energy relative to the ionic ground state; all lines from the Xe-II-20 and Xe-II-21 levels are too weak to be observed.

No	Configuration	Term	J	E (eV)	λ (nm)
Xe-II-1	$5p^4(^3P_2)6p$	² [3] ^o	7/2	14.098	484.4, 699.1
Xe-II-2	$5p^4(^3P_2)6p$	² [3] ^o	5/2	14.074	541.9, 553.1, 572.0
Xe-II-3	$5p^4(^3P_2)6p$	² [2] ^o	5/2	13.881	529.2, 605.1
Xe-II-4	$5p^4(^3P_2)6p$	² [2] ^o	3/2	13.860	533.9, 597.7, 609.8
Xe-II-5	$5p^4(^3P_2)6p$	² [1] ^o	3/2	14.479	460.3, 714.9
Xe-II-6	$5p^4(^3P_2)6p$	² [1] ^o	1/2	14.094	537.2, 566.8
Xe-II-7	$5p^4(^3P_1)6p$	² [2] ^o	5/2	15.264	492.1, 680.6
Xe-II-8	$5p^4(^3P_1)6p$	² [2] ^o	3/2	15.282	526.0, 577.6
Xe-II-9	$5p^4(^3P_1)6p$	² [1] ^o	3/2	15.410	575.1
Xe-II-10	$5p^4(^3P_1)6p$	² [1] ^o	1/2	15.445	754.8
Xe-II-11	$5p^4(^3P_1)6p$	² [0] ^o	1/2	15.024	543.9
Xe-II-12	$5p^4(^3P_0)6p$	² [1] ^o	3/2	15.080	488.4
Xe-II-13	$5p^4(^3P_0)6p$	² [1] ^o	1/2	14.930	519.1
Xe-II-14	$5p^4(^1D_2)6p$	² [3] ^o	7/2	16.126	487.7, 575.9, 659.5
Xe-II-15	$5p^4(^1D_2)6p$	² [3] ^o	5/2	15.978	627.1, 716.5
Xe-II-16	$5p^4(^1D_2)6p$	² [2] ^o	5/2	16.392	572.7
Xe-II-17	$5p^4(^1D_2)6p$	² [2] ^o	3/2	16.356	526.2
Xe-II-18	$5p^4(^1D_2)6p$	² [1] ^o	3/2	16.077	497.3, 597.1
Xe-II-19	$5p^4(^1D_2)6p$	² [1] ^o	1/2	16.458	504.5
Xe-II-20	$5p^4(^1S_0)6p$	² [1] ^o	3/2	18.497	
Xe-II-21	$5p^4(^1S_0)6p$	² [1] ^o	1/2	18.378	

$$e + Xe^+ \rightarrow e + Xe^{+*};$$
 (5)

$$e + Xe^* \rightarrow e + Xe^{**}; \tag{6}$$

$$e + Xe^{+*} \rightarrow e + Xe^{+**};$$
 (7)

$$e + Xe \rightarrow e + Xe^{+*}$$
. (8)

Here e denotes the electron, Xe is the neutral xenon atom in ground state, Xe^{*} is the atom in an excited state, Xe^{**} is the atom in a higher excited state; Xe⁺ is the xenon ion in its ground state, Xe^{+*} is the xenon ion in excited state, and Xe^{+**} is the xenon ion in a higher excited state. In this work, the characteristics of the excited states are analyzed according to the percentage contribution of these three groups of processes (i.e. ξ_{gs} , ξ_{ms} , and ξ_{i-e}). The line-ratios are selected for the diagnostics based on these parameters. In the following part of this section, the kinetic characteristics of several representative excited states are analyzed. The selection of line-ratios will be described in detail in section 2.3.

Figure 1 displays the variation of the percentage contributions with the ionization fraction and the electron temperature for three typical atomic excited states (Xe-I-3, Xe-I-6, and Xe-I-7 of table 1). It is seen that for the energy level Xe-I- 3, when the electron temperature and the ionization fraction are both low ($T_{\rm e} < 4~{\rm eV}$, $x_{\rm e} < 1\%$), ground-state excitation is significant in the population of this level, while increasing the electron temperature and the ionization fraction can both enhance the significance of the transitions between excited states. Panels (b) and (e) show that ground-state excitation always dominate the population of energy level Xe-I-6 in the parameter range investigated in the present work. Finally, panels (c) and (f) show that the dominant process of populating Xe-I-7 depends on the ionization fraction. When this fraction is smaller than 0.5%, ground-state excitation dominates the population. Contribution of this process decrease as $x_{\rm e}$ increases, and transitions between excited levels become the dominant process.

Figure 2 displays the variation of the percentage contribution with the ionization fraction and the electron temperature for three typical ionic excited levels (Xe-II-1, Xe-II-3, and Xe-II-5 of table 2). From panels (a), (d), and (g), it can be seen that both ground-state excitation and transitions between excited levels are important for the population of Xe-II-1 for most conditions ($x_e > 1.4\%$ or $T_e < 6$ eV); ionization–excitation becomes important in the upper left corner of the parameter space ($T_e > 6$ eV, $x_e < 1.4\%$).

Panels (b), (e), and (h) show that ionization–excitation is more important for the Xe-II-3 level than for Xe-II-1. This process contributes more than 70% in the triangle area at the upper left side of the parameter space (where $T_{\rm e}$ is high and

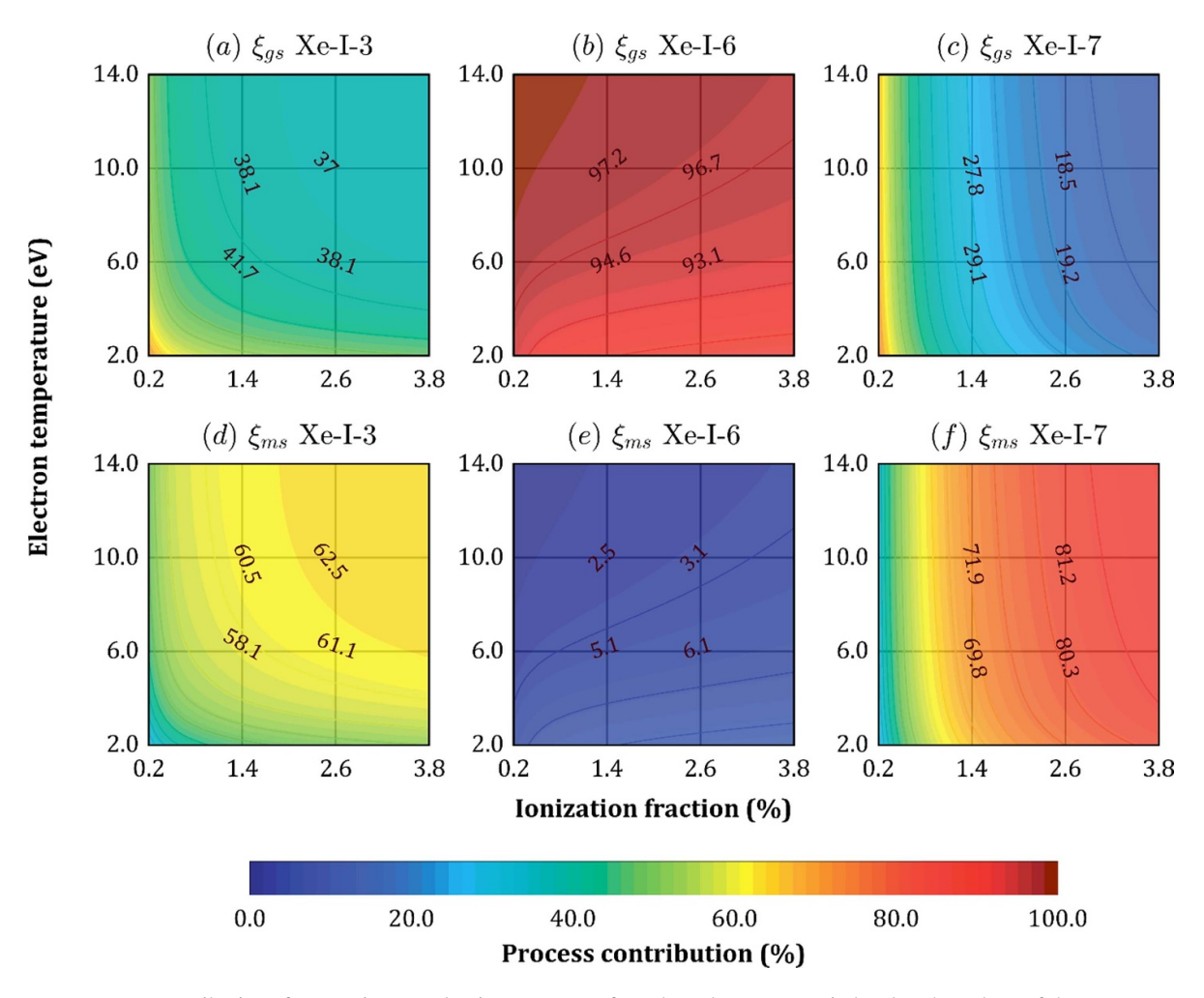


Figure 1. Percentage contributions from various production processes for selected xenon atomic levels. The values of the percentage contribution are shown as pseudo-colors. All the panels share the same colormap. Panels (a), (b), and (c) show the percentage contribution of the electron-induced ground state excitation (ξ_{gs}) for these levels, while panels (d), (e), and (f) present the percentage contribution of electron-induced transitions between excited states (ξ_{ms}). ξ_{i-e} is not shown in this figure because ξ_{i-e} should always be zero for the atomic levels.

 $x_{\rm e}$ is low). This area is much larger than that of level Xe-II-1. In the remaining parameter space, ground-state excitation and transitions between excited levels contribute nearly equally. Panels (c), (f), and (i) show that the production of Xe-II-5 is dominated by ground-state excitation, while ionization-excitation barely contributes in the parameter range investigated in the present work. Transitions between excited level contribute less than 30% in most areas. $\xi_{\rm ms}$ increases as $T_{\rm e}$ decreases and $x_{\rm e}$ increases. The maximum value of $\xi_{\rm ms}$ is \sim 28% at $T_{\rm e}=2$ eV, $x_{\rm e}=3.8\%$.

Above the dominant processes involving all 6p levels of the xenon atom and ion were analyzed. From those we can deduce the characteristics of the spectral lines emitted by these levels. Based on this information, section 2.3 will introduce the principle of selecting line-ratios and present the diagnostic method for determining ionization fraction.

2.3. Diagnostic method

According to the analysis presented in section 2.2, the spontaneous radiation dominates the de-population process of the ionic and atomic 6p levels in the parameter range investigated in the present work. The rate balance equation of the levels dominated by ground-state excitation can be approximately written as:

$$n_j \cdot \sum_{i} A_{j \to i} = \frac{n_e \cdot n_{gs} \cdot Q_{gs \to j}}{\xi_i^{gs}}.$$
 (9)

Here n_j is the density of level j, $A_{j\rightarrow i}$ is the Einstein coefficient of transition $j\rightarrow i$. $n_{\rm gs}$ is the ground-state density in either the ionic or neutral species. $Q_{{\rm gs}\rightarrow j}$ is the rate coefficient for the excitation process of level j from the ground state. $\xi_i^{\rm gs}$ is the percentage contributions of ground-state excitation

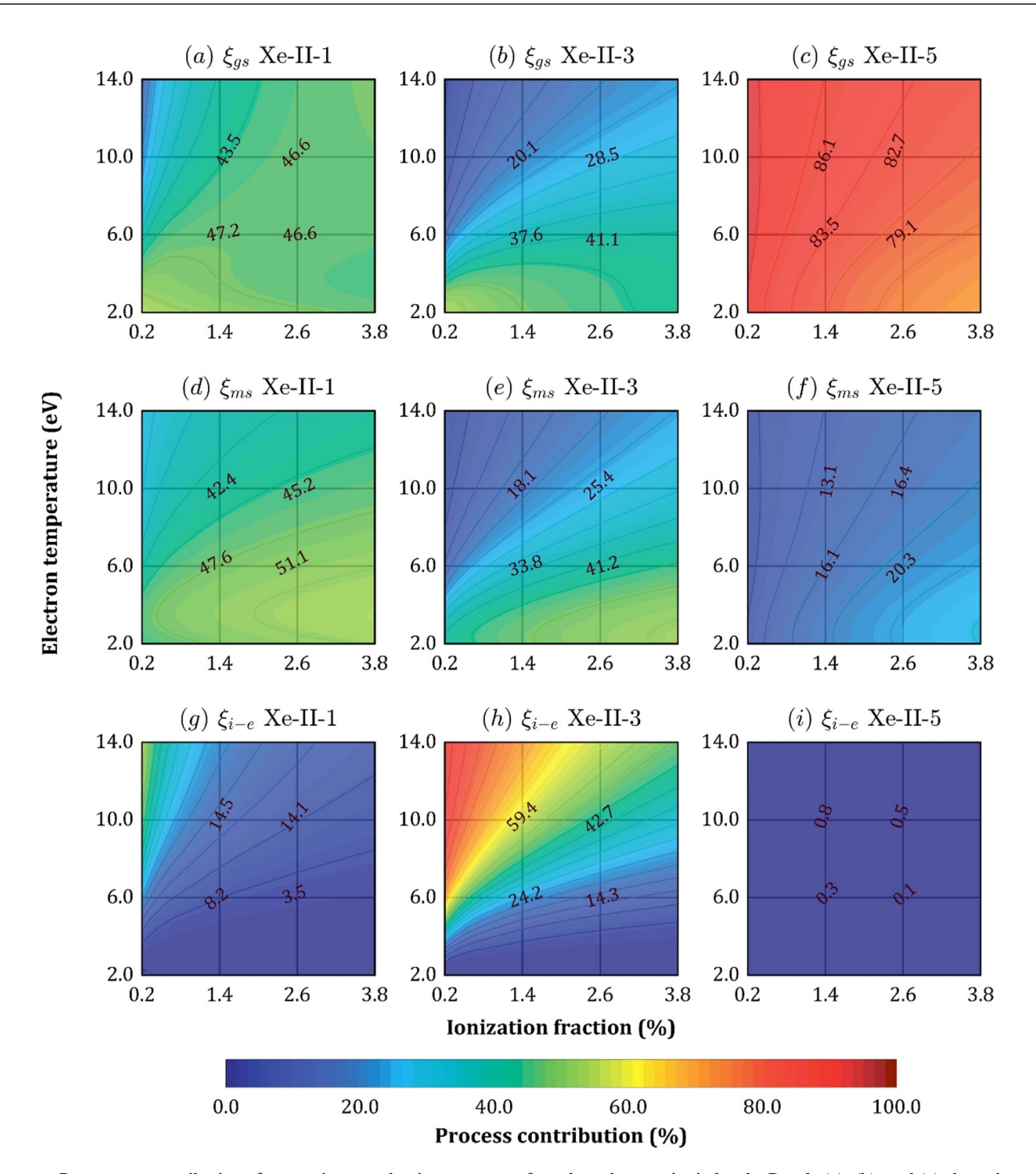


Figure 2. Percentage contributions from various production processes for selected xenon ionic levels. Panels (a), (b), and (c) show the percentage contribution from the ground-state excitation (ξ_{gs}); panels (d), (e), and (f) exhibit the percentage contribution of the transitions between excited states (ξ_{ms}); and panels (g), (h), and (i) show the percentage contribution of the electron-induced ionization–excitation process.

on level *i*. The spontaneous emission intensity $I_{j\rightarrow i}$ can be written as:

$$I(\lambda_{j\to i}) = n_j \cdot A_{j\to i} = \frac{n_e \cdot n_{gs} \cdot Q_{gs\to j} \cdot \mathcal{B}_{j\to i}}{\xi_i^{gs}}.$$
 (10)

Here $\lambda_{j\to i}$ is the wavelength of the transition $j\to i$, and $\mathcal{B}_{j\to i}$ is the branching ratio including the influence of self-absorption. Thus, for the ionic line λ_1 and the atomic line λ_2 that are both dominated by process (i), the line-ratio \mathcal{R}_{12} can be written as:

$$\mathcal{R}_{12} = \frac{I(\lambda_1)}{I(\lambda_2)} = \frac{n_{\text{ion}} \cdot Q_1 \cdot \mathcal{B}_1}{n_{\text{atom}} \cdot Q_2 \cdot \mathcal{B}_2} = x_e \cdot C \cdot \frac{Q_1}{Q_2} \cdot \frac{\xi_2^{\text{gs}}}{\xi_1^{\text{gs}}}. \tag{11}$$

Here the constant C is the ratio of the branching ratios, which can be calculated from the Einstein coefficients; $n_{\rm ion}$ and $n_{\rm atom}$ are the ionic and atomic densities. While, strictly speaking, $n_{\rm gs}$ in equations (9) and (10) are the atomic and ionic ground-state densities, considering that the density of the excited species is several orders of magnitude smaller than the ground-state density of the discharge device used in this work, we have $n_{\rm gs} \sim n_{\rm atom}$ for the atom and $n_{\rm gs} \sim n_{\rm ion}$ for the ion in equation (11).

It can be seen from the above description that equation (9) depends on the percentage contribution of ground-state excitation. We define a governing degree χ to evaluate the influence of ground-state excitation on the line-ratios as follows:

$$2/\chi = 1/\xi_1^{gs} + 1/\xi_2^{gs}.$$
 (12)

Here $\xi_1^{\rm gs}$ and $\xi_2^{\rm gs}$ are the percentage contributions of ground-state excitation on the numerator and the denominator of the line-ratio. The governing degree is defined as the harmonic mean rather than arithmetic or geometric means to reflect the influence of extremely small values better. When χ is 100%, the line-ratio is completely determined by ground-state excitation. Thus, one should choose line-ratios with the χ value as large as possible to reduce the uncertainty in the results. The governing degrees of line-ratios consisting of atomic and ionic 6p lines are calculated based on the CRM, and the results are presented in section 4.1.

Taking the rate coefficients in the Arrhenius form of equation (13), the ratio of the rate coefficients in equation (11) is a function of electron temperature and can be written as in equation (14) below:

$$Q = Q_{\rm c} \cdot \exp\left(-\frac{E_{\rm a}}{T_{\rm e}}\right),\tag{13}$$

$$\frac{Q_1}{Q_2} = \frac{Q_{c1}}{Q_{c2}} \cdot \exp\left(\frac{E_{a2} - E_{a1}}{T_e}\right). \tag{14}$$

Here $Q_{\rm c}$ is the rate constant and $E_{\rm a}$ is the activation energy, which both are determined by the feature of the energy level. The difference in the activation energy $\Delta E_{\rm a} = E_{\rm a1} - E_{\rm a2}$ reflects the extent to which the line-ratio is affected by the electron temperature. In order to reduce the influence of possible uncertainties in the electron temperature on the diagnostic result for the ionization fraction, one should choose line-ratios with a $\Delta E_{\rm a}$ value as small as possible.

From equations (11) and (14), it follows that the line-ratio of the ionic and atomic energy levels that are dominated by ground-state excitation is approximately a function of the ionization fraction and the electron temperature. Considering that the threshold energies for 'ground-state excitation', 'transition between excited levels', and 'ionization-excitation' are quite

different, the line-ratios from energy levels that are dominated by different processes are sensitive to the electron temperature. Actually, the OES method based on this ideology has been developed and widely used to determine the electron temperature in the study of xenon plasmas [27–29]. By using the two types of line-ratios above, the ionization fraction can be determined.

3. Experiment

3.1. Measurement of plasma emission spectra

This section introduces the discharge chamber and the experimental setup. A magnetized DC discharge chamber is employed in this work. The chamber has two layouts: a cusped-field layout shown in figure 3(a) and an axial-field layout exhibited in figure 3(b).

The cusped-field layout consists of a hollow cathode, three ring magnets, a cylindrical anode, and a quartz bucket. The ring magnets are installed with the same poles opposite to each other, thereby forming a cusped magnetic field configuration in the discharge chamber. Figure 3(a) also shows the magnetic lines of the cusped field, as calculated by an axisymmetric finite-element magnetic model simulation [51]. The cylindrical anode has a diameter of 90 mm and a length of 86 mm. An 8 mm wide window is designed along the direction parallel to the axis on the anode for spectral measurements. The quartz bucket is installed outside the cylindrical anode to avoid gas leakage from the window. Figure 3(b) shows the structure of the axial-field discharge chamber. Eight bar magnets are installed along the direction parallel to the axis instead of ring magnets, which generate an axial magnetic field as depicted in the figure. All other settings are the same as in the cusped-field layout.

The emission spectrum is measured using a Horiba FHR-1000 spectrometer with a Synapse charged-coupled device (CCD) detector. In the experiment, the slit of spectrometer is set to 20 μ m. The spectral resolution at 400–1000 nm is better than 0.05 nm. The relative spectral response of the optical system was calibrated with a tungsten halogen lamp before the experiment. A ceramic optical probe (inner diameter \sim 2 mm, length \sim 8 cm) is mounted perpendicular to the axis of the discharge chamber. A Langmuir probe is inserted in the discharge chamber shown in figure 1 from the exit. Step motors are used to drive the Langmuir probe and the optical probe to move along the axial direction of the discharge chamber. In the experiment, the measuring point at z=35 mm is blocked by a ring magnet. Thus, no spectrum is measured at this point.

Figure 4 displays a typical emission spectrum measured in the discharge chamber. Actually, some Xe-I (8d), Xe-I (6f), Xe-I (7p), and Xe-II (7s) lines are also observed in the spectrum, but only the dominant groups are indicated here. The Xe-II (6p) lines are dominant in the visible range (450–700 nm), while most of the Xe-I (6p) lines are in the range of 750–950 nm.

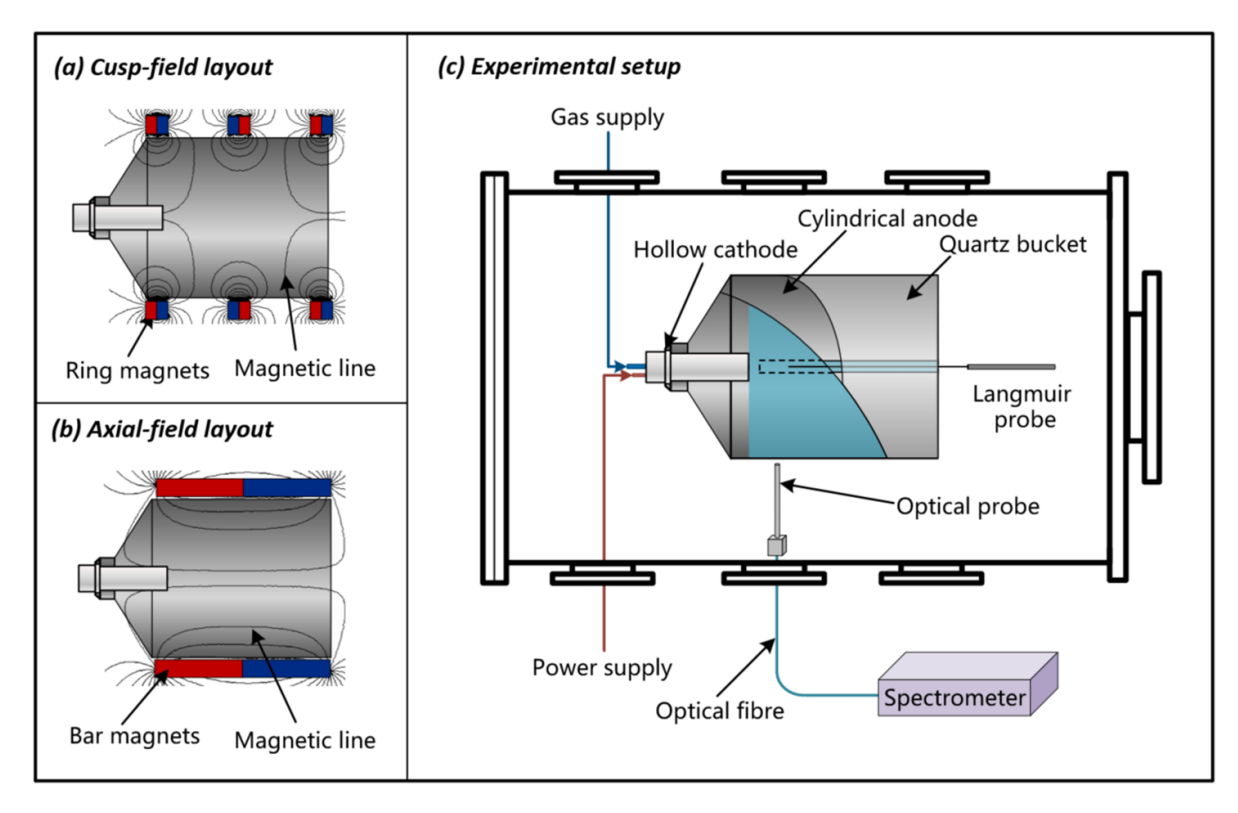


Figure 3. Schematic diagram of (a) the cusped-field discharge chamber, (b) the axial-field discharge chamber, and (c) the experimental setup.

3.2. Determination of ionization fraction using the Langmuir probe

A Langmuir probe is employed to compare with the OES method. This section presents the details of using the Langmuir probe to determine the ionization fraction. The Langmuir probe used in this work has a circular plane electrode with a diameter of \sim 0.3 mm. The current collected by the probe in the electron retarding region can be written as:

$$\mathcal{J}(U_{\rm p}) = \frac{e \cdot n_0}{4} \cdot \sqrt{\frac{2 \cdot e}{m_{\rm e}}} \cdot S \cdot \int_{U_{\rm s} - U_{\rm p}}^{\infty} \sqrt{E_{\rm e} - (U_{\rm s} - U_{\rm p})}$$
$$\cdot f_{\rm EEDF}(E_{\rm e}) \cdot dE_{\rm e} - \mathcal{J}_{\rm i}. \tag{15}$$

Here \mathcal{J} is the probe current, U_p is the probe voltage, e represents the elementary charge, n_0 denotes the plasma density, m_e is the mass of electron, S is the electrode area of the probe, U_s is the space potential, E_e is the electron energy, \mathcal{J}_i is the ion current, and f_{EEDF} is the electron energy distribution function. In this work, a two-parameter electron energy distribution function (EEDF) is utilized in the fitting procedure [52], which is:

$$f_{x}(E_{e}) = p_{1} \cdot T_{x}^{-3/2} \cdot \sqrt{E_{e}} \cdot e^{-p_{2} \cdot (E_{e}/T_{x})^{x}},$$
 (16)

where,

$$p_1 = x \left(\frac{2}{3}\right)^{3/2} \cdot \frac{\left[\Gamma\left(\frac{5}{2x}\right)\right]^{3/2}}{\left[\Gamma\left(\frac{3}{2x}\right)\right]^{5/2}},\tag{17}$$

$$p_2 = \left(\frac{2}{3}\right)^x \cdot \left[\frac{\Gamma\left(\frac{5}{2x}\right)}{\Gamma\left(\frac{3}{2x}\right)}\right]^x. \tag{18}$$

Here Γ is the Gamma function, T_x is an effective temperature which has $T_x = (2/3)\bar{E}_e$, where \bar{E}_e is the average electron energy. A Maxwellian distribution corresponds to the case of x = 1; while a Druyvesteyn distribution corresponds to x = 2. The plasma density is determined by fitting the voltage–current curve with equation (15) as done in [53] (shown in figure 5).

On the other hand, a free molecular model is utilized to obtain the spatially-resolved atom density in the discharge chamber, which employs the angular coefficient method to perform the calculation [54, 55]. The ionization fraction is then determined from the probe measured plasma density and the simulated atom density, and compared with the OES method in section 4.2.

3.3. Investigation on spatial resolution of the optical probe

In section 3.1, an optical probe is utilized in the experiment to measure the axially-resolved spectra of a magnetized discharge chamber. In this section, we investigate the spatial resolution of the optical probe. A Tungsten lamp (diameter ~ 5 mm) is utilized as dot source. It is mounted on a

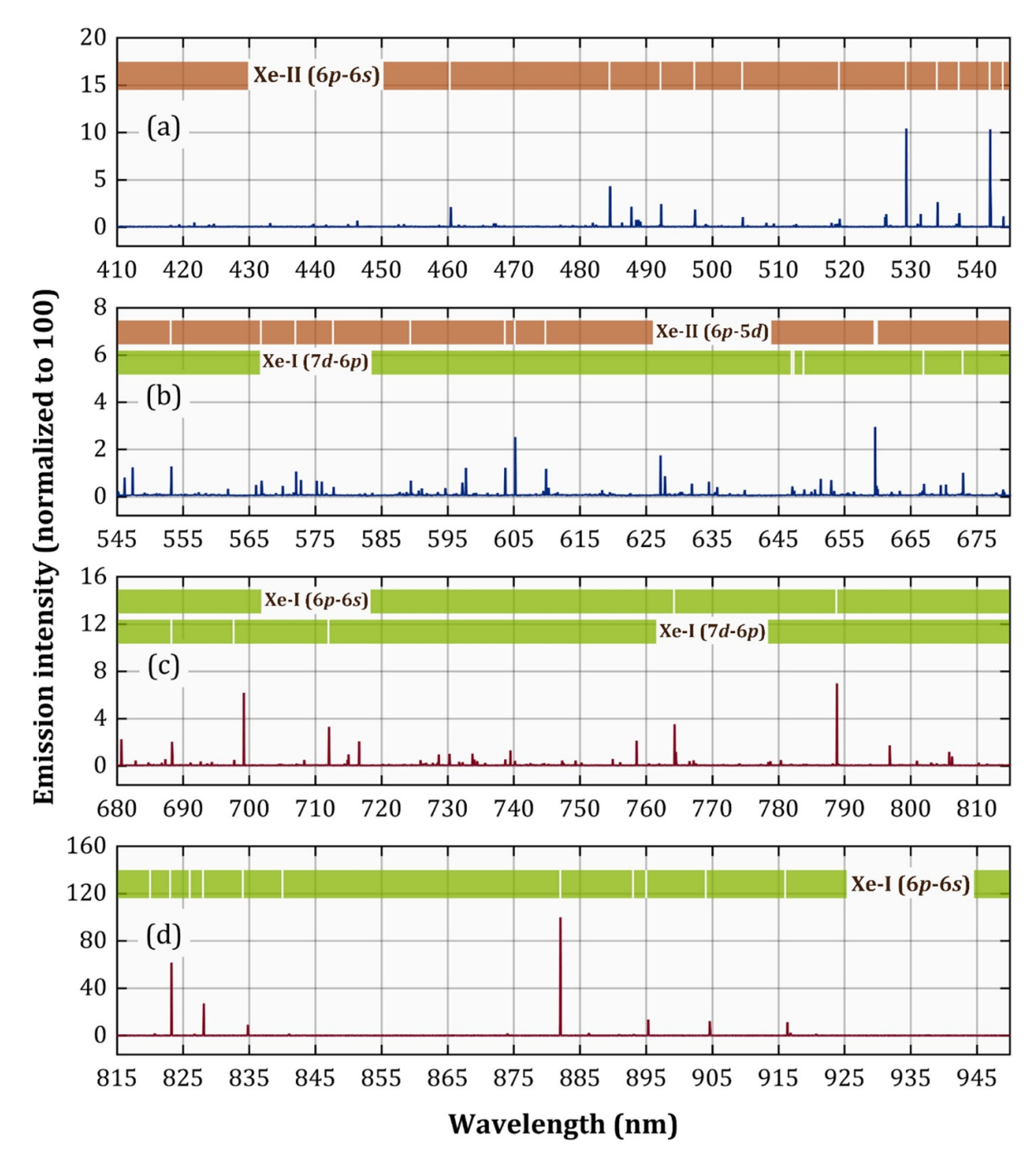


Figure 4. Typical emission spectrum in the discharge chamber. The upper and lower energy levels of the emission lines are indicated in the strips at the top of the subfigures. The emission lines are grouped according to the configuration of the upper and lower levels. The short vertical lines in the strips mark the emission lines belonging to the corresponding line group.

translation stage and can be moved perpendicular to the lineof-sight of the optical probe. The optical probe is connected to the spectrometer utilizing the same optical fiber used in section 3.1. A diagram of the experiment setup is given in figure 6(a). The experiment is conducted with different d (the distance from the tungsten lamp to the optical probe).

The objective of this experiment is to measure the instrument function P(z) of the optical probe by moving the dot

source in direction z perpendicular to the line of sight of the optical probe. The emission intensity measured along z-direction is $E_p(z)$. The spatial distribution of the emission intensity of the Tungsten lamp T is measured using a CMOS camera. When the dot source locates at $z=z_0$, we have:

$$E_{\rm p}(z_0) = \int_{-\infty}^{+\infty} T(z - z_0) \cdot P(z) \cdot \mathrm{d}z. \tag{19}$$

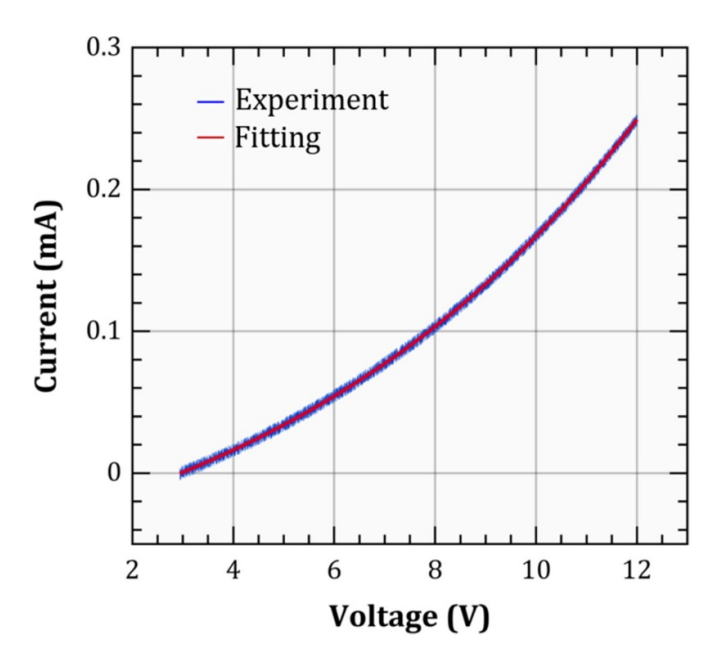


Figure 5. A typical fitting result of the electron retarding region of the voltage–current curve measured by the Langmuir probe.

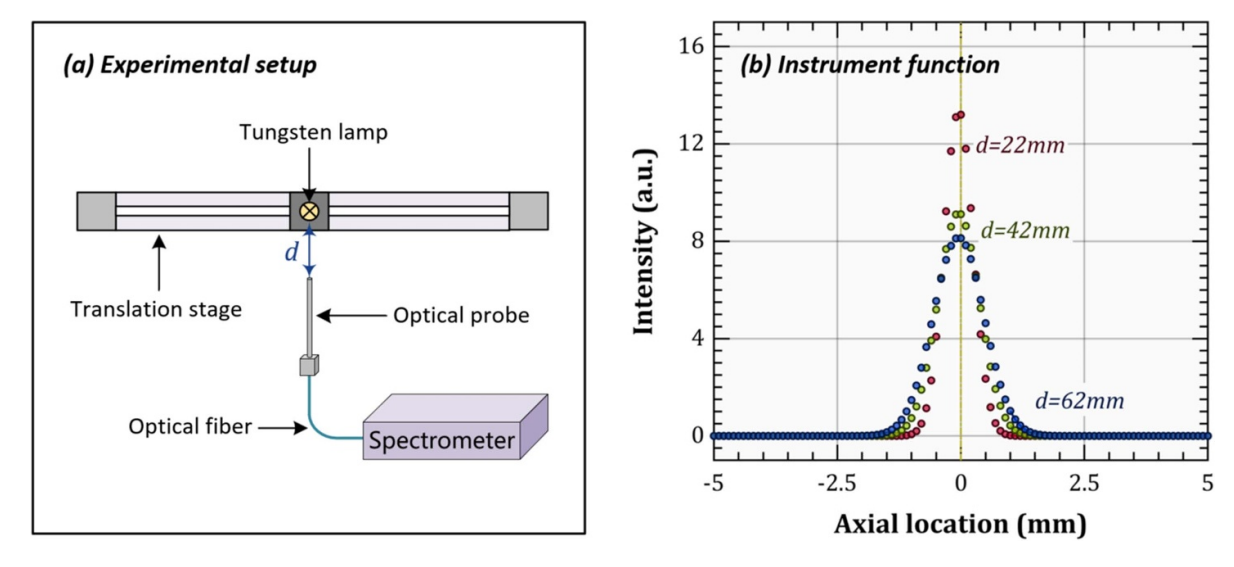


Figure 6. (a) Diagram of the experiment for spatial resolution of the optical probe. (b) The instrument function of the optical probe measured in this work. d is the distance between the tungsten lamp and the optical probe.

The instrument function P(z) can thus be obtained by deconvolution of E_p and T (figure 6(b)). It shows that the angular resolution of the optical probe is $\sim 1^{\circ}$, and the spatial-resolution is better than 2 mm along the axis of the discharge chamber.

In the measurement of the plasma spectrum, the composition of emission intensity along the line-of-sight direction is a significant problem that restricts the spatial resolution of plasma measurement. A variety of experimental techniques and data analysis methods have been developed to achieve spatial resolution in this direction [56, 57]. The optical probe used in this work lacks spatial-resolution ability along the line-of-sight direction. The intensity measured by this probe is the

integral value of the plasma emission in the visual cone of the probe. However, it is found that the plasma near the axis is far more ablaze than that near the cylindrical wall during the experiment.

Figure 7(a) presents the normalized emission intensity of the plasma along the radial direction of the discharge chamber. The circle and the square with guided lines in figure 7(a) denote the radial intensity distribution of the axial-field and the cusp-field layouts. The emission intensity is extracted from pictures taken along the axis of the discharge chamber. By integrating the emission intensity along the radial direction, we can analyze the contribution of a certain region to the total integral intensity. Figure 7(b) presents the integrated intensity

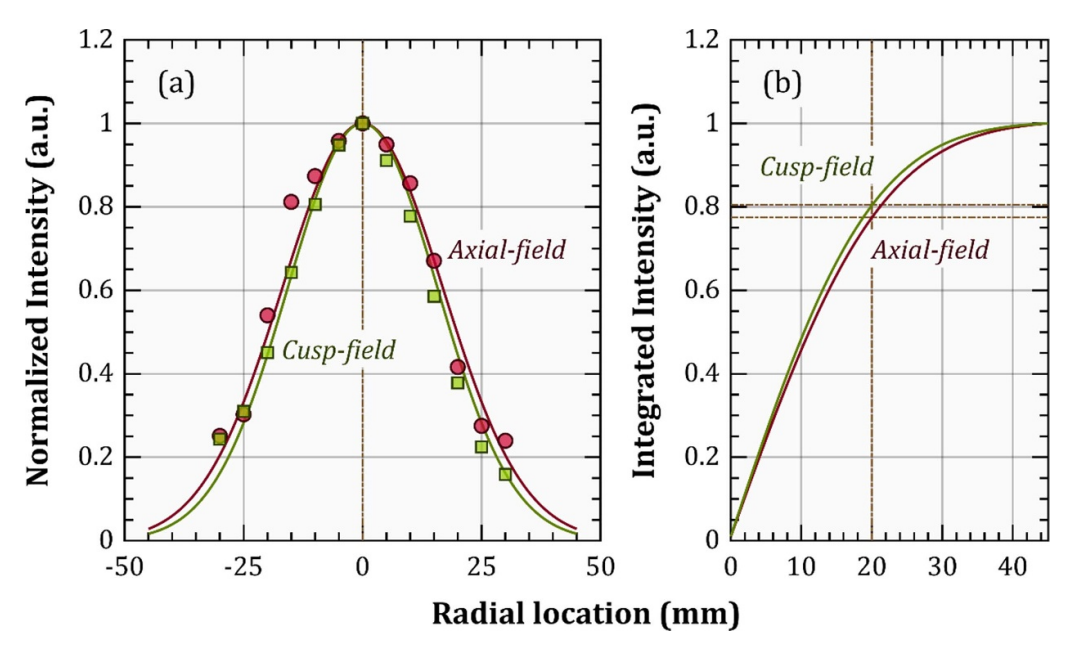


Figure 7. (a) Radial distribution of normalized emission intensity in the magnetized discharge chamber. (b) Variation of the line-integrated intensity along the radius of the discharge chamber.

along the radial direction. The integrated intensity is calculated using equation (20):

$$\gamma(r_0) = \frac{\int_0^{r_0} \mathbf{T}(r) \cdot dr}{\int_0^{r_d} \mathbf{T}(r) \cdot dr}.$$
 (20)

Here $\gamma(r_0)$ is the normalized integrated intensity at $r=r_0$, T(r) is the plasma emission intensity at radial position r, and $r_{\rm d}$ is the radius of the discharge chamber. Figure 7(b) shows that for the cusp-field layout, about 80% of the total emission intensity is emitted by the plasma in the area with r<20 mm. In comparison, over 75% of the total emission intensity is emitted by the plasma in the area with r<20 mm for the axial-field layout.

According to Langmuir probe measurements in similar discharge chamber [58, 59], the electron density (n_e) , electron temperature (T_e) , and atom density (n_a) decrease along the radial direction in this kind of discharge chambers. Considering the line intensities utilized in this work are positively correlated with the n_e , T_e , and n_a (equation (10)), the intensities should also decrease along the radial direction. This means the emission lines utilized in this work have similar intensity profiles as figure 7(a). Thus, the result from the OES method can be regarded as the ionization fraction of the plasma near the axis weighted by emission intensity, which is also one of the important sources of difference in comparison with the Langmuir probe.

4. Results

Using the OES method presented in section 2, the ionization fraction along the axis of a magnetized discharge chamber (described in section 3) is determined. Section 4.1 presents the results for and a discussion regarding the selection of appropriate line-ratios. Section 4.2 compares the ionization fraction

from the OES method with that obtained from a Langmuir probe. In section 4.3, the axial distributions of the ionization fraction in different magnetic fields (a cusped-field layout and an axial-field layout) are investigated. Section 4.4 analyzes the relationship between the line-ratios and the ionization fraction, from which a simplified scheme is obtained. This simplified scheme enables a fast estimate of the ionization fraction.

4.1. Selection of line-ratios

Table 3 gives the $\Delta E_{\rm a}$ and governing degree χ of the lineratios made up from ionic and atomic 6p levels. The governing degree is an evaluation of the influence of ground-state excitation on the line-ratio, which is defined in equation (12). It indicates the error caused by the approximation introduced in equation (9). The larger the value of χ , the smaller the error introduced. $\Delta E_{\rm a}$ implies the dependence of the line-ratio on the electron temperature. According to equation (13), the smaller the value of $\Delta E_{\rm a}$, the less the lineratio is influenced by the electron temperature. The governing degree presented in table 3 are given for $T_{\rm e}=8$ eV and $x_{\rm e}=2\%$.

We calculated the governing degree χ of the line-ratios made up of all the 21 ionic 6p levels and the ten atomic 6p levels in the ionization fraction range of $x_{\rm e} \sim 0.2\%-3.8\%$, i.e. the electron temperature range $T_{\rm e} \sim 2-14$ eV. The lineratios with governing degree χ consistently better than 60% are listed in the table. These line-ratios are all closely related to the ionization fraction, and hence they can be used in the diagnostics. However, considering the differences in the signal-to-noise ratio of these emission lines, we choose the line-ratios of 460.303 nm to 828.011 nm and 754.603 nm to 828.011 nm for our diagnostics of the ionization fraction.

Table 3. Governing degree χ and activation energy difference ΔE_a of line-ratios made up from emission lines emitted by ionic and atomic 6p levels.

Ionic energy level			Atomic energy level				
Configuration	Term	J	Configuration	Term	\overline{J}	χ	$\Delta E_{\rm a}~({\rm eV})$
$5p^4(^3P_2)6p$	² [1] ^o	3/2	$5p^5(^2P^{\circ}_{3/2}) 6p$	² [1/2]	0	70	2.3
$5p^4(^3P_1)6p$	² [1] ^o	3/2	$5p^5(^2P^{o}_{3/2}) 6p$	² [1/2]	0	60	5.5
$5p^4(^3P_1)6p$	² [1] ^o	1/2	$5p^5(^2P^{o}_{3/2})$ 6p	² [1/2]	0	82	5.5
$5p^4(^3P_1)6p$	² [0] ^o	1/2	$5p^5(^2P^o_{3/2})$ 6p	² [1/2]	0	62	5.1
$5p^4(^3P_0)6p$	² [1] ^o	1/2	$5p^5(^2P^{o}_{3/2}) 6p$	² [1/2]	0	60	5.1
$5p^4(^1D_2)6p$	² [3] ^o	5/2	$5p^5(^2P^{o}_{3/2})$ 6p	² [1/2]	0	70	6
$5p^4(^1D_2)6p$	² [2] ^o	5/2	$5p^5(^2P^o_{3/2})$ 6p	² [1/2]	0	64	6.5
$5p^4(^1D_2)6p$	² [1] ^o	3/2	$5p^5(^2P^{o}_{3/2}) 6p$	² [1/2]	0	75	6.1
$5p^4(^1D_2)6p$	² [1] ^o	1/2	$5p^5(^2P^0_{3/2})$ $6p$	² [1/2]	0	60	6.5
$5p^4(^3P_1)6p$	² [1] ^o	1/2	$5p^5(^2P^0_{1/2})$ 6p	² [1/2]	0	67	4.3
$5p^4(^1D_2)6p$	² [1] ^o	3/2	$5p^5(^2P^0_{1/2})$ 6p	² [1/2]	0	62	4.9

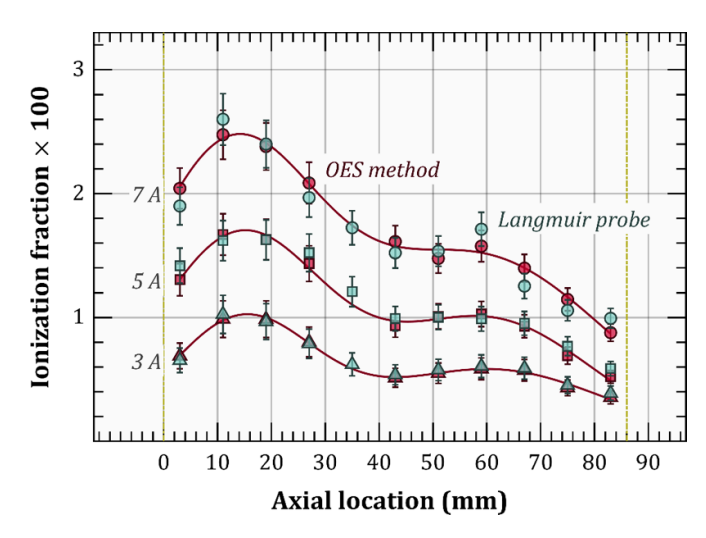


Figure 8. Ionization fraction obtained by the OES method and a Langmuir probe in the cusped-field discharge chamber. The gas flow rates of the three working conditions are 3 SCCM. The discharge currents are 7 A, 5 A, and 3 A, respectively. The exit of the cathode locates at z=0 mm. The ionization fraction determined by the OES method is connected using a fitting line. Since the measured point at $z\sim35$ mm is blocked by a ring magnet, there is no OES result at this position.

The scheme for determining the electron temperature is the same as used in [29]. It was found that the ionic levels listed in table 3 all have total electronic angular momentum of J=3/2 or 1/2, while the atomic levels have J=0, i.e. these levels have the same total angular momentum as the respective ionic and atomic ground states. We will discuss this phenomenon from the perspective of atomic physics in section 5.1.

4.2. Comparison between OES results and Langmuir probe results

Figure 8 compares the ionization fraction measured by the OES method with that of a Langmuir probe for three operating conditions of cusped-field discharge chambers. As denoted in figure 8, the discharge currents of the three operating conditions are 7 A, 5 A, and 3 A, respectively; the gas flow rate of these operating conditions is 3 SCCM. The ionization fraction

of 11 measured points along the axis of the discharge chamber are compared. The error bars in figure 8 reflect the uncertainty of the measurement.

Figure 8 shows that the ionization fraction increases as the discharge current increases; the increasing ratio of the ionization fraction is consistent with that of the discharge current. Considering that the discharge current implies the total amount of electrons/ions in the plasma and the neutral density is determined by the gas flow rate, which is same for these three conditions, this phenomenon is in accordance with the physical expectation. It demonstrates that the ionization fractions measured in the present experiment are reasonable from another perspective.

Figure 9 compares the ionization fraction in three working conditions with the same discharge current of 7 A, while the gas flow rates are 3 SCCM, 5 SCCM, and 8 SCCM, respectively. The relationship between the ionization fraction and the current-to-flow ratio is also approximately linear

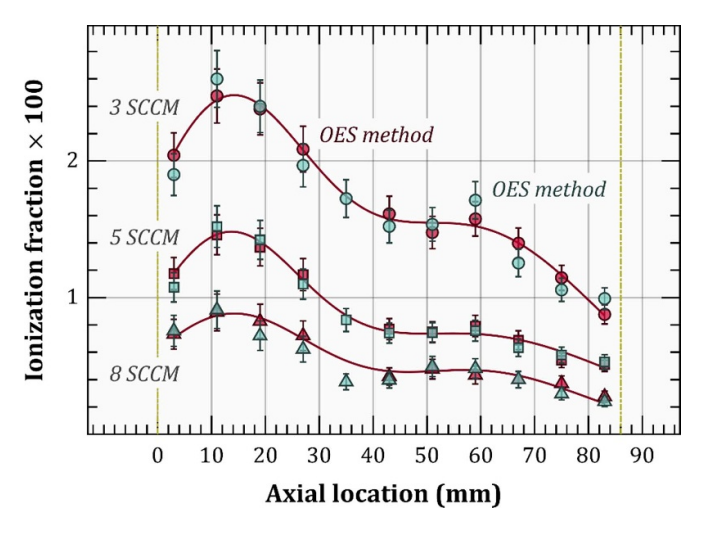


Figure 9. Ionization fraction obtained by the OES method and a Langmuir probe in the cusped-field discharge chamber. The discharge currents of the three working conditions are 7 A. The gas flow rates are 3 SCCM, 5 SCCM, and 8 SCCM, respectively.

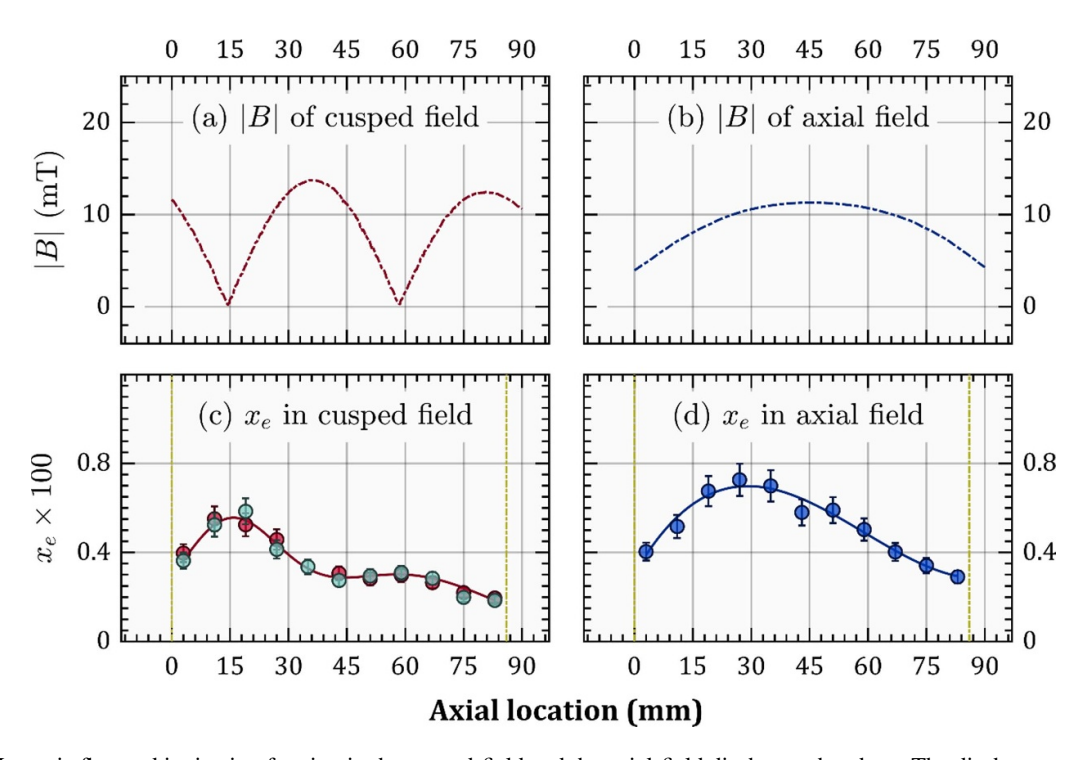


Figure 10. Magnetic flux and ionization fraction in the cusped-field and the axial-field discharge chambers. The discharge current is 3 A, and the gas flow rate is 5 SCCM.

for these three conditions. The maximum ionization fractions under these operating conditions are 2.5%, 1.5%, and 0.9%, respectively.

Figures 8 and 9 show that the axial distribution of the ionization fraction in the cusped-field discharge chamber is biconvex. The two peaks locate at $z \sim 14$ mm and $z \sim 60$ mm, while the valley between the two peaks locates at $z \sim 40$ mm for all the operating conditions. These positions are consistent with the two minimum points and the one maximum point of the magnetic flux on the axis. This implies that the distribution of the ionization fraction depends on the topology of the magnetic field in a cusped-field discharge chamber.

Further investigations regarding the relationship between the ionization fraction and the magnetic field are carried out in section 4.3.

The uncertainty of the OES results in figures 8 and 9 is evaluated by considering the following factors: (a) the uncertainty in spectral measurement; (b) the uncertainty introduced by the approximation of equation (9) due to contribution of processes other than electron-induced excitation from the ground state; (c) the residual error associated with multi-line-ratio fitting. The uncertainty in spectral measurement can be determined from the noise-to-signal ratio of emission lines. The experimental data show that noise affects the ionic lines more

significantly. For instance, the ionic 460.30 nm line's noise-to-signal is $\sim 3\%-10\%$, while the noise-to-signal ratio is $\sim 1\%-3\%$ for the atomic 828.01 nm line. The uncertainty introduced by equation (9) can be evaluated from the percentage contribution of ground-state excitation ξ^{gs} . For the intensity ratio of 460.03 nm to 828.01 nm line, ground-state contributions are $\xi^{gs}_{460} \sim 80\%-86\%$ (uncertainty $\sim 6\%$), and $\xi^{gs}_{828} \sim 93\%-97\%$ (uncertainty $\sim 4\%$). Thus the combined uncertainty introduced by this term is $\sim 7\%$. The uncertainty induced by the residual error is $\sim 5\%$. The combined uncertainty of the OES method is $\sim 13\%$.

The uncertainty of the Langmuir probe is evaluated by considering: (a) the uncertainty from atom density distribution (\sim 5%); (b) the uncertainty induced by voltage–current curve measurement (\sim 10%); (c) the residual error associated with voltage–current curve fitting (\sim 5%). The combined uncertainty of the Langmuir probe is \sim 11%.

The EEDF in the discharge chamber of ion thrusters may be non-Maxwellian [10, 60]. By fitting the voltage–current curve measured by the Langmuir probe (figure 5), it is found that the EEDF in the cusp-field discharge chamber indeed deviates slightly from a Maxwellian distribution. The uncertainty in the EEDF may also affect the diagnostic result. In the present work, the line-ratios with small activation energy difference ΔE_a are adopted to minimize the influence of the EEDF. Considering that the dominant processes have different threshold energies, the spectral lines emitted by these levels can reflect the proportion of electrons with different energies. It is indeed possible to evaluate the EEDF using the OES method [61, 62].

4.3. Investigation on the relationship between ionization fraction and magnetic field

Figure 10 shows the axial distribution of the ionization fraction and the magnetic flux on the axis of the discharge chamber. Panel (a) exhibits the magnetic flux of the cusped-field discharge chamber, while panel (b) displays the magnetic flux in the axial-field discharge chamber. Panels (c) and (d) present the ionization fraction of the cusped-field and axial-field layouts, respectively. Both layouts share the same discharge current and gas flow rate of 7 A and 5 SCCM.

For the axial-field layout, we do not have results from the Langmuir probe for comparison, because the probe tip in the experiment reached a white-hot state and burned down very quickly. A possible reason is that the axial magnetic field configuration forms a magnetic nozzle along the axis of the discharge chamber, which then accelerates the ions. The accelerated ions then bombard the probe tip, thereby causing it to overheat quickly. Note that magnetic nozzles have been widely used to accelerate ions in various electric propulsion devices, e.g. micro-cathode-arc thrusters and ECR plasma thrusters [63, 64].

Comparing the ionization fraction with the magnetic flux of the cusped-field layout, it is apparent that the peaks of the ionization fraction nearly have the same positions as the valleys of the magnetic flux. This is probably due to the constraint of the magnetic field on the electrons. The electrons emitted from the cathode are confined by the magnetic field to move along the magnetic field lines. Magnetic fields of ring magnets squeeze together, forming magnetic mirrors at $z \sim 15$ mm and $z \sim 58$ mm. Since the electrons are constrained in this area, there is a better chance for collisions with the atom. On the other hand, electrons can move along the magnetic line to radial distances around $z \sim 15$ mm and $z \sim 58$ mm. This extends the overall path of the electrons to the anode and also enhances the collision. Thus, the ionization fraction increases around these positions.

Comparing panels (c) and (d), it is found that the ionization fraction of the axial-field layout is generally larger than that of the cusped-field layout, under the same discharge current and gas flow rate. More specifically, the ionization fraction is almost equal before the first peak of the cusped-field layout, while the ionization fraction of the axial-field layout keeps getting larger than that of the cusped-field layout in other positions. The possible reason is that the electrons are constrained near the axis of the discharge chamber in the axial-field layout, while the electrons in the cusped field move along the radial direction around the valley of the magnetic field. Thus, the ionization fraction on the axis of the axial field is larger than in the cusped field.

4.4. Fast determination of ionization fraction

Figure 11 shows the relationship between the ionization fraction and three typical line-ratios of ionic to atomic lines.

To simplify the narrative, we define: (I) the energy level that is predominantly excited by electron collisions from ground the state as 'ground-dominated level'; (II) the energy level that is predominantly populated by electron-induced transitions between excited species as 'transition-dominated level'. The three line-ratios are representatives of: ratios of two 'grounddominated levels' (460.30 nm to 828.01 nm in panel (a)), ratios of a 'transition-dominated level' to a 'ground-dominated level' (529.22 nm to 828.01 nm in panel (b)), and ratios of a 'grounddominated level' to a 'transition-dominated level' (460.30 nm to 823.16 nm in panel (c)). One should note that the lineratios presented in panels (b) and (c) are made up of different emission lines rather than simply inversely proportional to each other. The data points given in this figure are measured at different positions in the discharge chamber. The data points with low x_e that agree with the curve with $T_e = 10$ eV are mainly located on the far side of the hollow cathode; while the data points that agree with the curve with $T_{\rm e}=5~{\rm eV}$ are measured near the hollow cathode. This phenomenon means electron temperature increases with the distance from the hollow cathode.

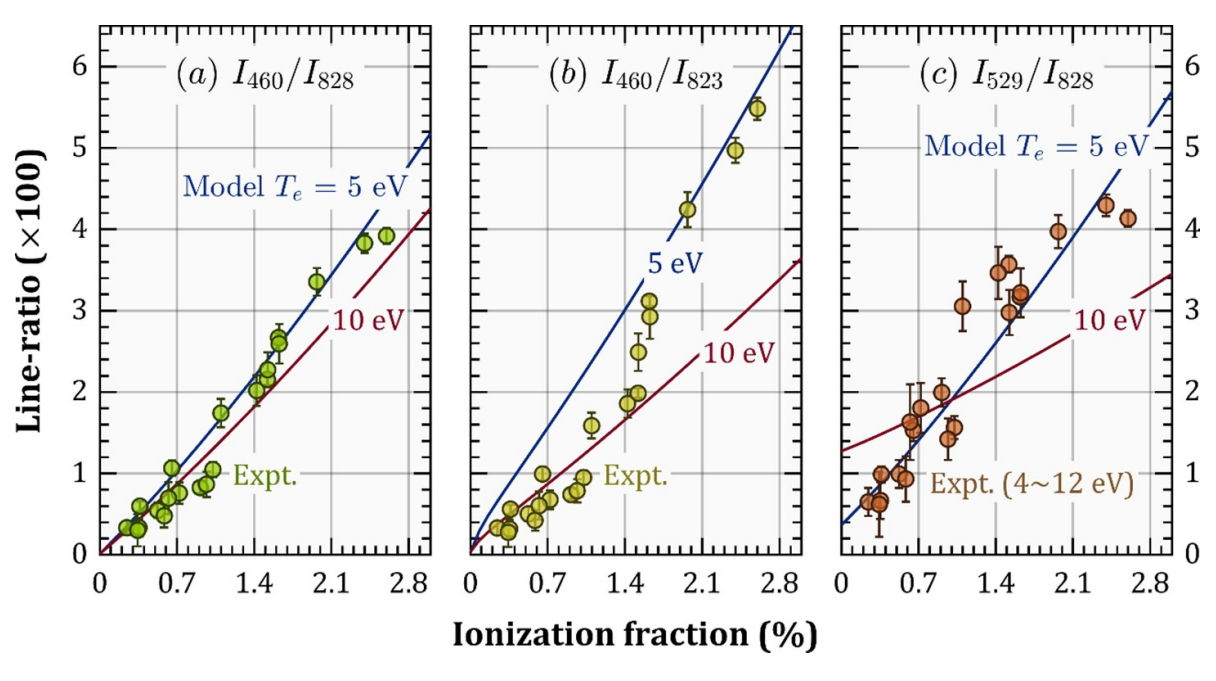


Figure 11. Variation of three typical line-ratios with the ionization fraction. The circles are the measured data. The solid line are the results calculated by the comprehensive model assuming the electron temperature is either 5 eV or 10 eV.

We note that the line-ratio in panel (a) is less sensitive to the electron temperature compare with panels (b) and (c). The relationship show in panel (a) is approximately linear. The relationship between the ionization fraction and the lineratio shown in panel (b) is monotonously increasing, but it is affected significantly by electron temperature. The electron temperature and ionization fraction of the plasma can be determined simultaneously using the line-ratios represented in panels (a) and (b). The relationship of the ionization fraction to the line-ratio shown in panel (c) is more complex: this line-ratio increases with the electron temperature when the ionization fraction is low ($x_e < 1\%$), but decreases when the ionization fraction is larger than 1%. Therefore, using the line-ratios represented in panel (c) in OES diagnostics is more complicated.

Actually, the line-ratio shown in panel (a) can also have a clear correlation with the electron temperature when this temperature is very low, as becomes evident by considering the difference in the activation energy $\Delta E_{\rm a} \sim 2.3$ eV for this lineratio. As the electron temperature increases, the dependence on that temperature weakens, and the relationship between the ionization fraction and the line-ratio becomes approximately linear. In this case, the effect of the electron temperature may be ignored, and the ionization fraction can be quickly estimated using equation (21) below. The parameters c_1 in equation (21) can be taken as 0.597 for the line-ratio of 460.30 nm to 828.01 nm $\mathcal{R}_{460/828}$. Hence:

$$x_{\rm e} \approx c_1 \cdot \mathcal{R}_{460/828}.\tag{21}$$

Note that equation (21) is more accurate when the electron temperature is relatively high ($T_e > 5$ eV).

The fast determination scheme of equation (21) is obtained by neglecting the influence of electron temperature on the lineratio of 460.30 nm to 828.01 nm lines. From this perspective, the fast determination scheme can be regarded as a simplified form of equation (11) derived from the CRM. Considering the upper levels of 460.03 nm and 828.01 nm lines are dominated by electron-impact excitation and spontaneous radiation process, the dimension and geometry of the chamber have no significant influence on the fast determination scheme. The fast determination scheme can be applied to other plasmas if the plasma meets the applicability range presented in section 5.2. One should note that a reconstruction of emission intensity distribution along the line-of-sight may be needed before using the scheme. Otherwise, the result will be an intensity-weighted mean value, as in this work.

5. Discussions

5.1. Discussion of the relationship between the dominant process and the quantum numbers

The present work focuses on the diagnostics of the ionization fraction. Some special line-ratios that have sensitive relationships to the ionization fraction are used in the diagnostics. The spectral lines constituting these line-ratios are emitted by ionic and atomic 6p levels. According to the above analysis, these excited levels are dominated by electron-induced excitation processes from the respective atomic and ionic ground states. This indicates the importance of finding energy levels that are dominated by ground-state excitation. These levels can be utilized for developing similar diagnostic methods for other gases (e.g. helium, argon, krypton, and iodine plasmas) as in the work reported here. By finding such levels of ions with higher ionization stages (e.g. Xe^{2+} , Xe^{3+}), the diagnostic method

to determine the relative fraction of these ions could also be developed. This would be highly beneficial for the development of plasma devices in general.

Table 3 shows that the energy levels that are dominated by ground-state excitation share a common feature: they have the same total electronic angular momentum J as their respective ground states. This rule applies to both the atom and the ion. Similar phenomena were also observed in the atomic energy levels of argon and krypton [46, 65]. On the other hand, considering that the metastable states have the maximum density in the excited state (it can be 2–3 orders higher than that of other excited levels), the reaction rates for processes out of a metastable state are very important for analyzing the dominant processes for an excited level.

According to our comprehensive CRM, metastable excitation processes are indeed important for some energy levels but not important for others. Among the latter levels, some of them also share the same J with the ground state. Transitions between the metastable and these other levels, however, are optically (spin-)forbidden. Usually, electron-impact cross sections for these transitions are significantly smaller than for transitions that are optically (spin- and parity-) allowed, except very close to threshold in some cases. Some studies clearly show that the size of the electron-impact cross section is indeed related to whether the dipole transition between the two levels is forbidden [66, 67]. In the cases of interest for the present work, however, even though the one-electron transition 5p-6ptransition is optically forbidden, if the initial and the final states are otherwise identical with respect to their quantum numbers, the transition resembles some characteristics of elastic scattering. Hence, some of these cross sections tend to be significantly larger than one might expect otherwise. This is, indeed, confirmed by the ab initio BSR calculations that are the basis of our CRM.

5.2. The applicability range of the OES method

Section 4.4 presents a fast determination method for ionization fraction which utilizes the line-ratio of ionic 460.30 nm line to atomic 828.01 nm line. The fast method depends on the specific kinetics of the excited levels selected, i.e. the dominancy of the ground-state excitation process in the production of these levels. Thus, it is applicable in a specific parameter range. When the ionization fraction is extremely low $(x_{\rm e} < 10^{-4})$, the ionization–excitation process can become important for the upper level of 460.30 nm. In this case, the rate balance equation for this level cannot be written as equation (9), the fast determination method can no longer be used. For a given gas pressure, increase of ionization fraction leads to higher electron density and higher electron collision frequency, which will make the collision process play a more important role in the de-population of excited species. When de-population rate through collision is comparable to spontaneous radiation ($n_e > 5 \times 10^{12} \text{ cm}^{-3}$), equation (10) will introduce an evident deviation.

It can also be seen from equations (11)–(14) that the line-ratio is determined by both the ionization fraction and the electron temperature. For plasma with electron temperature $T_{\rm e} > 4$ eV, the rate-coefficient ratio does not change significantly with electron temperature. In this range, the diagnostic error introduced by electron temperature is acceptable (\sim 15%). However, the error will increase rapidly as the electron temperature decreases. In the above range of plasma parameters, a comprehensive CRM should be used and a formal multi-parameter fitting technique should be adopted to determine the ionization fraction.

6. Conclusion

We have presented an OES method for determining the ionization fraction in a xenon plasma by using ionic and atomic lines from the 6p states. Based on a comprehensive CRM, we analyzed the dominant kinetic process of the ionic and atomic 6p energy levels. Line-ratios with a sensitive relationship to the ionization fraction were selected, which are the basis of the OES method developed here. The validity of the OES method is demonstrated with a magnetized discharge chamber, where the predictions are examined by comparing them with the ionization fraction obtained from a Langmuir probe. We also investigated the relationship between the axial distribution of the ionization fraction and the magnetic field configuration. In addition, a simplified scheme for the fast determination of ionization fraction was reported, and the possibility of extending the OES method to plasmas of other gas was discussed. The OES method presented in this paper can be used to determine the ionization fraction of electric propulsion devices.

Data availability statement

All data that support the findings of this study are included within the article (and any supplementary files).

Acknowledgments

The authors would like to express their gratitude to Mr. Yuan-He Zhang for his help in the experiment. We also thank the editors for helpful suggestions to improve the initial draft of the manuscript. This work was financially supported by the National Natural Science Foundation of China under Grant No. U22B2094, and by the United States National Science Foundation under Grants Nos. OAC-1834740 and PHY-2110023.

Appendix

This appendix lists all the atomic and ionic energy levels in the CR model in tables A1 and A2.

Table A1. The atomic levels included in the CR model. E_b is the bound energy of the levels.

No.	Energy level	E _b (eV)	No.	Energy level	E _b (eV)
1	$5s^25p^{61}S_0$	0	34	$5p^5 (^2P^o_{1/2}) 6p^2 [3/2]_2$	11.0547
2	$5p^5(^2P^{o}_{3/2})6s^2[3/2]^{o}_2$	8.3153	35	$5p^5 (^2P^o_{3/2}) 6d^2 [5/2]^o_2$	11.0648
3	$5p^5(^2P^o_{3/2})6s^2[3/2]^o_1$	8.4365	36	$5p^5 (^2P^0_{1/2}) 6p^2 [1/2]_1$	11.0691
4	$5p^5(^2P^o_{1/2}) 6s^2[1/2]^o_0$	9.4472	37	$5p^5 (^2P^{o}_{3/2}) 6d^2 [5/2]^{o}_3$	11.1009
5	$5p^5 (^2P^o_{1/2}) 6s^2 [1/2]^o_1$	9.5697	38	$5p^5 (^2P^0_{1/2}) 6p^2 [1/2]_0$	11.1412
6	$5p^5 (^2P^o_{3/2}) 6p^2 [1/2]_1$	9.5802	39	$5p^5 (^2P^o_{3/2}) 6d^2[3/2]^o_1$	11.1626
7	$5p^5 (^2P^o_{3/2}) 6p^2 [5/2]_2$	9.6856	40	$5p^5 (^2P^{o}_{3/2}) 8s^2 [3/2]^{o}_2$	11.2583
8	$5p^5 (^2P^o_{3/2}) 6p^2 [5/2]_3$	9.7207	41	$5p^5 (^2P^o_{3/2}) 4f^2 [3/2]_1$	11.2627
9	$5p^5 (^2P^o_{3/2}) 6p^2 [3/2]_1$	9.7893	42	$5p^5 (^2P^o_{3/2}) 4f^2[3/2]_2$	11.2639
10	$5p^5 (^2P^o_{3/2}) 6p^2 [3/2]_2$	9.8211	43	$5p^5 (^2P^o_{3/2}) 4f^2 [9/2]_5$	11.2653
11	$5p^5 (^2P^o_{3/2}) 5d^2[1/2]^o_0$	9.8904	44	$5p^5 (^2P^o_{3/2}) 4f^2 [9/2]_4$	11.2654
12	$5p^5 (^2P^o_{3/2}) 5d^2[1/2]^o_1$	9.9171	45	$5p^5 (^2P^o_{3/2}) 4f^2 [5/2]_3$	11.271
13	$5p^5 (^2P^0_{3/2}) 6p^2 [1/2]_0$	9.9335	46	$5p^5 (^2P^o_{3/2}) 4f^2 [5/2]_2$	11.2714
14	$5p^5 (^2P^o_{3/2}) 5d^2 [7/2]^o_4$	9.9431	47	$5p^5 (^2P^o_{3/2}) 8s^2 [3/2]^o_1$	11.2742
15	$5p^5 (^2P^0_{3/2}) 5d^2[3/2]^0_2$	9.9588	48	$5p^5 (^2P^0_{3/2}) 4f^2 [7/2]_3$	11.2756
16	$5p^5 (^2P^o_{3/2}) 5d^2 [7/2]^o_3$	10.0391	49	$5p^5 (^2P^o_{3/2}) 4f^2 [7/2]_4$	11.2756
17	$5p^5 (^2P^o_{3/2}) 5d^2 [5/2]^o_2$	10.1575	50	$5p^5 (^2P^o_{1/2}) 5d^2 [5/2]^o_2$	11.3015
18	$5p^5 (^2P^o_{3/2}) 5d^2 [5/2]^o_3$	10.22	51	$5p^5 (^2P^o_{1/2}) 5d^2 [3/2]^o_2$	11.338
19	$5p^5 (^2P^0_{3/2}) 5d^2[3/2]^0_1$	10.401	52	$5p^5 (^2P^o_{1/2}) 5d^2 [5/2]^o_3$	11.3751
20	$5p^5 (^2P^0_{3/2}) 7s^2 [3/2]^0_2$	10.5621	53	$5p^5 (^2P^{o}_{3/2}) 7d^2 [1/2]^{o}_1$	11.4225
21	$5p^5 (^2P^0_{3/2}) 7s^2 [3/2]^0_1$	10.5932	54	$5p^5 (^2P^o_{3/2}) 8p^2 [1/2]_1$	11.4256
22	$5p^5 (^2P^0_{3/2}) 7p^2 [1/2]_1$	10.9016	55	$5p^5 (^2P^o_{3/2}) 8p^2 [5/2]_2$	11.434
23	$5p^5 (^2P^0_{3/2}) 7p^2 [5/2]_2$	10.9542	56	$5p^5 (^2P^o_{3/2}) 7d^2 [1/2]^o_0$	11.4388
24	$5p^5 (^2P^0_{1/2}) 6p^2 [3/2]_1$	10.9576	57	$5p^5 (^2P^o_{3/2}) 8p^2 [5/2]_3$	11.4394
25	$5p^5 (^2P^0_{3/2}) 7p^2 [5/2]_3$	10.9688	58	$5p^5 (^2P^o_{3/2}) 8p^2 [3/2]_1$	11.4478
26	$5p^{5} (^{2}P^{o}_{3/2}) 6d^{2} [1/2]^{o}_{0}$	10.9715	59	$5p^5 (^2P^o_{3/2}) 8p^2 [3/2]_2$	11.4525
27	$5p^5 (^2P^0_{3/2}) 6d^2[1/2]^0_1$	10.9788	60	$5p^5 (^2P^{\circ}_{3/2}) 7d^2 [7/2]^{\circ}_4$	11.4617
28	$5p^5 (^2P^0_{3/2}) 7p^2 [3/2]_2$	10.9957	61	$5p^5 (^2P^o_{3/2}) 8p^2 [1/2]_0$	11.4754
29	$5p^5 (^2P^0_{3/2}) 6d^2[3/2]^0_2$	10.9984	62	$5p^5 (^2P^{\circ}_{3/2}) 7d^2 [7/2]^{\circ}_3$	11.4867
30	$5p^5 (^2P^0_{3/2}) 7p^2 [3/2]_1$	11.0029	63	$5p^5 (^2P^0_{3/2}) 7d^2 [5/2]^0_2$	11.4907
31	$5p^5 (^2P^0_{3/2}) 7p^2 [1/2]_0$	11.015	64	$5p^{5} (^{2}P^{o}_{3/2}) 7d^{2} [3/2]^{o}_{1}$	11.4951
32	$5p^5 (^2P^0_{3/2}) 6d^2[7/2]^0_4$	11.0236	65	$5p^5 (^2P^{\circ}_{3/2}) 7d^2 [3/2]^{\circ}_2$	11.496
33	$5p^5 (^2P^o_{3/2}) 6d^2 [7/2]^o_3$	11.0377	66	$5p^5 (^2P^o_{3/2}) 7d^2 [5/2]^o_3$	11.4975

No. Energy level E_{b} (eV) Energy level $E_{\rm h}$ (eV) No. $5p^{5}{}^{2}P^{o}{}_{3/2}$ $5p^4 (^3P_2) 6p^2 [3]^{\circ}_{7/2}$ 1 0 31 14.0977 $5p^{5}{}^{2}P^{o}{}_{1/2}$ $5p^4 (^3P_2) 5d^2[3]_{5/2}$ 2 1.3064 14.2273 32 $5s5p^{6} {}^{2}S_{1/2}$ $5p^4 (^1D_2) 5d^2[4]_{9/2}$ 3 11.2669 33 14.2464 $5p^4$ (³P₂) 6s ²[2]_{5/2} $5p^4 (^1D_2) 5d^2[4]_{7/2}$ 4 11.539 34 14.2475 $5p^4 (^3P_2) 6s^2[2]_{3/2}$ $5p^4 (^3P_2) 6p^2 [1]^{\circ}_{3/2}$ 5 11.7865 35 14.4793 $5p^4 (^3P_2) 5d^2[2]_{5/2}$ $5p^4$ (1D_2) $5d^2[3]_{5/2}$ 6 11.8277 36 14.7647 $5p^4 (^3P_2) 5d^2[3]_{7/2}$ $5p^4 (^3P_2) 6p^2 [1]^{o}_{1/2}$ 7 37 11.8328 14.9295 $5p^4 (^3P_2) 5d^2[2]_{3/2}$ $5p^4 (^1D_2) 5d^2[3]_{7/2}$ 8 11.9066 38 14.9839 $5p^4 (^3P_2) 5d^2[1]_{1/2}$ $5p^4 (^3P_2) 6p^2 [0]^{o}_{1/2}$ 9 12.0089 39 15.0244 $5p^4 (^3P_2) 5d^2[4]_{9/2}$ $5p^4 (^3P_2) 6p^2 [1]^{o}_{3/2}$ 10 12.3246 40 15.0801 $5p^4 (^3P_2) 6s^2[0]_{1/2}$ $5p^4 (^3P_2) 6p^2 [2]^{\circ}_{5/2}$ 11 12.5419 41 15.264 $5p^4 (^3P_2) 5d^2[4]_{7/2}$ $5p^4 (^3P_2) 6p^2 [2]^{\circ}_{3/2}$ 12 12.5888 42 15.2816 $5p^4 (^3P_2) 6s^2 [1]_{3/2}$ $5p^4 (^1D_2) 5d^2[1]_{3/2}$ 13 12.7455 43 15.3827 $5p^4 (^3P_2) 5d^2[1]_{1/2}$ 14 12.9254 44 $5p^4 (^3P_2) 6p^2 [1]^{\circ}_{3/2}$ 15.4099 $5p^4 (^3P_2) 5d^2[1]_{3/2}$ 15 13.0572 45 $5p^4$ (1D_2) $5d^2[2]_{5/2}$ 15.4115 16 $5p^4 (^3P_2) 5d^2[0]_{1/2}$ 13.1358 46 $5p^4 (^3P_2) 6p^2 [1]^{\circ}_{1/2}$ 15.4448 17 $5p^4$ (³P₂) $5d^2$ [3]_{5/2} 13.2012 47 $5p^4$ (1D_2) $5d^2[1]_{1/2}$ 15.7473 $5p^4 (^1D_2) 5d^2[2]_{3/2}$ $5p^4 (^3P_2) 6s^2 [1]_{1/2}$ 13.2547 48 18 15 8114 $5p^4 (^3P_2) 5d^2[2]_{3/2}$ 13.3136 49 $5p^4 (^1D_2) 6p^2 [3]^{\circ}_{5/2}$ 15.9775 19 $5p^4 (^3P_2) 5d^2[1]_{3/2}$ 13.3785 50 $5p^4$ (1S_0) $6s^2[0]_{1/2}$ 20 16.0248 $5p^4 (^3P_2) 5d^2[2]_{5/2}$ 13.3912 $5p^4 (^1D_2) 6p^2 [1]^{\circ}_{3/2}$ 21 51 16.0767 $5p^4 (^3P_2) 5d^2[3]_{7/2}$ $5p^4 (^1D_2) 6p^2 [3]^{o}_{7/2}$ 13.4427 22 52 16.1259 $5p^4$ (1D_2) $6s^2[2]_{5/2}$ $5p^4 (^1D_2) 6p^2 [2]^o_{3/2}$ 23 13.5841 53 16.3565 $5p^4 (^3P_2) 5d^2[2]_{3/2}$ $5p^4 (^1D_2) 6p^2 [2]^{o}_{5/2}$ 13.8028 54 24 16.3917 $5p^4 (^3P_2) 6p^2 [2]^{\circ}_{3/2}$ $5p^4 (^1D_2) 6p^2 [1]^o_{1/2}$ 25 55 13.8605 16.4578 $5p^4 (^3P_2) 6p^2 [2]^{o}_{5/2}$ $5p^4 (^1D_2) 5d^2[0]_{1/2}$ 26 13.8811 56 16.7454 $5p^4 (^3P_2) 5d^2[2]_{5/2}$ $5p^4$ (1S_0) $5d^2[2]_{5/2}$ 27 13.9735 57 16.9325 $5p^4 (^1D_2) 6s^2 [2]_{3/2}$ $5p^4$ (1S_0) $5d^2[2]_{3/2}$ 14.0009 58 28 17.1176 $5p^4 (^3P_2) 6p^2 [3]^{\circ}_{5/2}$ $5p^4 (^1S_0) 6p^2 [1]^0_{1/2}$ 29 14.0737 59 18.3775 30 $5p^4 (^3P_2) 6p^2 [1]^{\circ}_{1/2}$ 14.0936 $5p^4 (^1S_0) 6p^2 [1]^{\circ}_{3/2}$ 18.4974

Table A2. The ionic levels included in the CR model. $E_{\rm b}$ is the bound energy of the levels.

ORCID iDs

Xi-Ming Zhu https://orcid.org/0000-0002-6501-0096 Yan-Fei Wang https://orcid.org/0000-0002-9226-8279 Sheng-Feng Meng https://orcid.org/0009-0002-6007-8435

Klaus Bartschat https://orcid.org/0000-0001-6215-5014

References

- [1] Liu W, Cai G B, Zhang J R, Xia G Q and Wang W Z 2021 Numerical investigation of plasma behavior in a micro DC ion thruster using the particle-in-cell/Monte Carlo collision (PIC/MCC) method J. Phys. D: Appl. Phys. 54 445202
- [2] Shirakawa R, Yamashita Y, Koda D, Tsukizaki R, Shimizu Y, Tagawa M and Nishiyama K 2020 Investigation and experimental simulation of performance deterioration of microwave discharge ion thruster μ10 during space operation Acta Astronaut. 174 367
- [3] Ferrer P and Tchonang M P 2011 Miniaturization of electrostatic ion engines by ionization and acceleration coupling J. Phys. D: Appl. Phys. 44 335204
- [4] Ryan W C and Richard E W 2013 Mission capability assessment of cubesats using a miniature ion thruster *J. Propul. Power* **50** 1035

- [5] Yamauchi T and Xu K G 2018 A miniature gridded ion thruster using split ring resonator microplasma AIAA Propulsion Energy Forum (Cincinnati, USA, 9–11 July) (https://doi.org/10.2514/6.2018-4651)
- [6] Ling L Y W, Zhang S, Fu H, Huang M C, Quansah J, Liu X Y and Wang N F 2020 A brief review of alternative propellants and requirements for pulsed plasma thrusters in micropropulsion applications *Chin. J. Aeronaut.* 33 2999
- [7] Nakamura K, Nakagawa Y, Koizumi H and Takao Y 2018 Numerical analysis of a miniature microwave-discharge ion thruster using water as the propellant *Trans. Jpn. Soc.* Aeronaut. Space Sci. 61 152
- [8] Koizumi H, Komurasaki K, Aoyama J and Yamaguchi K 2018 Development and flight operation of a miniature ion propulsion system J. Propul. Power 34 960
- [9] Holste K, Gartner W, Zschatzsch D, Scharmann S, Köhler P, Dietz P and Klar P J 2018 Performance of an iodine-fueled radio-frequency ion-thruster Eur. Phys. J. D 72 9
- [10] Masherov P E, Riaby V A and Godyak V A 2016 Integral electrical characteristics and local plasma parameters of a RF ion thruster Rev. Sci. Instrum. 87 02B926
- [11] Tani Y, Tsukizki R, Koda D, Nishiyama K and Kuninaka H 2019 Performance improvement of the μ 10 microwave discharge ion thruster by expansion of the plasma production volume *Acta Astronaut.* **157** 425
- [12] Xia X, Yang J, Jin Y Z, Hang G R, Fu Y L and Hu Z 2020 Vaccum 179 109517
- [13] Yeo S H, Ogawa H, Kahnfeld D and Schneider R 2021 Miniaturization perspectives of electrostatic propulsion

- for small spacecraft platforms *Prog. Aerosp. Sci.* **126** 100742
- [14] Jia L J, Yang L, Zhao Y, Liu M Z, Jia Y H, Zhang T P, Zhuang J H, Yang F Q, Zhao Y D and Wu X M 2019 An experimental study of a dual-stage 4-grid ion thruster *Plasma Sources Sci. Technol.* 28 105003
- [15] Desangles V, Milhone J, Cooper C, Weisberg D B, Nornberg M D and Forest C B 2018 High ionisation fraction plasmas in a low temperature, multidipole cusp plasma J. Plasma Phys. 84 905840312
- [16] Choueiri E and Lauro F 2022 Scaling of the ionization fraction in a self-field MPD thruster 37th Int. Electric Propulsion Conf. (Cambridge, USA, 19–23 June) (https://doi.org/ 10.1121/10.0014604)
- [17] Bernatova K, Fekete M, Klein P, Hnilica J and Vašina P 2020 Ionisation fractions of sputtered titanium species at target and substrate region in HiPIMS *Plasma Sources Sci. Technol.* 29 055010
- [18] Zuo X, Zhang D, Chen R D, Ke P L, Oden M and Wang A Y 2020 Spectroscopic investigation on the near-substrate plasma characteristics of chromium HiPIMS in low density discharge mode *Plasma Sources Sci. Technol.* 29 015013
- [19] Luo J, Chen L S, Duan H Z, Gong Y G, Hu S C, Ji J H, Liu Q, Mei J W, Milyukov V and Sazhin M 2016 TianQin: a space-borne gravitational wave detector *Class. Quantum Grav.* 33 035010
- [20] Vepa R 2020 Feedback control of a spacecraft electro-dynamic thruster Acta Astronaut. 172 82
- [21] Magaldi B, Karnopp J, Sobrinho A S and Pessoa R 2022 A global model study of plasma chemistry and propulsion parameters of a gridded ion thruster using argon as propellant *Plasma* 5 324
- [22] Tummala A R and Dutta A 2017 An overview of cube-satellite propulsion technologies and trends Aerospace 4 58
- [23] Butler A, Brenning N, Raadu M A, Gudmundsson J T, Minea T and Lundin D 2018 On three different ways to quantify the degree of ionization in sputtering magnetrons Plasma Sources Sci. Technol. 27 105005
- [24] Magee R M, Galante M E, Gulbrandsen N, McCarren D W and Scime E E 2012 Direct measurements of the ionization profile in krypton helicon plasmas *Phys. Plasma* 19 123506
- [25] Guo S L, Jin X L, Lei L and Li B 2019 Effects of magnetic field on plasma confinement of an ion thruster discharge chamber *IEEE Trans. Plasma Sci.* 49 3358
- [26] Ryabinkin A N, Serov A O, Pal A F, Mankelevich Y A, Rakhimov A T and Rakhimova T V 2021 Structure of DC magnetron sputtering discharge at various gas pressures: a two-dimensional particle-in-cell Monte Carlo collision study *Plasma Sources Sci. Technol.* 30 055009
- [27] Huang B D, Takashimma K, Zhu X M and Pu Y K 2015 The influence of the voltage rise rate on the breakdown of an atmospheric pressure helium nanosecond parallel-plate discharge J. Phys. D: Appl. Phys. 48 125202
- [28] Akatsuka H 2018 Optical emission spectroscopic (OES) analysis for diagnostics of electron density and temperature in non-equilibrium argon plasma based on collisional-radiative model Adv. Phys. X 4 1592707
- [29] Zhu X M, Walsh J L, Chen W C and Pu Y K 2012 Measurement of the temporal evolution of electron density in a nanosecond pulsed argon microplasma: using both Stark broadening and an OES line-ratio method J. Phys. D: Appl. Phys. 45 295201
- [30] Mishra H, Tichy M and Kudrna P 2022 Optical emission spectroscopy study of plasma parameters in low-pressure hollow cathode plasma jet and planar magnetron powered by DC and pulsed DC supply *Vacuum* 205 111413
- [31] Liu C, Tanaka N, Zhu B J, Nishihara K, Fujioka S, Kang K S, Suh Y D, Kim J G, Ozawa K and Kubo M 2022 Time-resolved measurement of radical populations in

- extreme-ultraviolet-light-induced hydrogen plasma *Appl. Phys. Express* **15** 036002
- [32] Zhu X M, Chen W C, Li J, Cheng Z W and Pu Y K 2012 Spatial evolution of the electron energy distribution function in a low-pressure capacitively coupled plasma containing argon and krypton *Plasma Sources Sci. Technol.* 21 045009
- [33] Tibere-Inglesse A C, McGuire S D, Mariotto P and Laux C O 2021 Measurements and analysis of rotational temperatures obtained with Raman and optical emission spectroscopy in a nonequilibrium nitrogen plasma *Plasma Sources Sci. Technol.* 30 125019
- [34] Zhu X M and Pu Y K 2010 Optical emission spectroscopy in low-temperature plasmas containing argon and nitrogen: determination of the electron temperature and density by the line-ratio method *J. Phys. D: Appl. Phys.* **43** 403001
- [35] Wei L Q, Li W B, Ding Y J, Zhu X M, Wang Y F, Hu J F, Yan S L and Yu D R 2018 Plasma Sources Sci. Technol. 27 084002
- [36] Han X, Zhang Z, Chen Z Y, Marano M, Tang H B and Cao J B 2021 High-spatial-resolution image reconstruction-based method for measuring electron temperature and density of the very near field of an applied-field magnetoplasmadynamic thruster J. Phys. D: Appl. Phys. 54 135203
- [37] Lu Q, Yuan B W, Song Y J, Yang Q, Qiao J J, Wang D Z and Xiong Q 2022 Characteristic diagnostics of a laser-stabilized high-pressure argon plasma by optical emission spectroscopy *IEEE Trans. Plasma Sci.* **50** 2578
- [38] Nauschuett B, Chen L M, Holste K and Klar P J 2022 Combination of optical emission spectroscopy and multivariate data analysis techniques as a versatile non-invasive tool for characterizing xenon/krypton mixed gas plasma inside operating ion thrusters *J. Appl. Phys.* 131 053301
- [39] Lee D, Doh G, Kim H, Garrigues L and Choe W H 2021 Distinct discharge modes in micro Hall thruster plasmas Plasma Sources Sci. Technol. 30 035004
- [40] Patrick D, Gartner W, Koch Q, Köhler P E, Teng Y, Schreiner P R, Holste K and Klar P J 2019 Molecular propellants for ion thrusters *Plasma Sources Sci. Technol.* 28 084001
- [41] Celik M 2011 Spectral measurements of inductively coupled and helicon discharge modes of a laboratory argon plasma source Spectrochim. Acta B 66 149
- [42] Karabadzhak G F, Chiu Y H and Dressler R A 2006 Passive optical diagnostic of Xe propelled Hall thrusters. II. Collisional-radiative model J. Appl. Phys. 99 113305
- [43] Wang Y, Wang Y F, Zhu X M, Zatsarinny O and Bartschat K 2019 A xenon collisional-radiative model applicable to electric propulsion devices: i. Calculations of electron-impact cross sections for xenon ions by the Dirac B-spline R-matrix method *Plasma Sources Sci. Technol.* 28 105004
- [44] Zhu X M, Wang Y F, Wang Y, Yu D R, Zatsarinny O, Bartschat K, Tsankov T V and Czarnetzki U 2019 A xenon collisional-radiative model applicable to electric propulsion devices: II. Kinetics of the 6s, 6p, and 5d states of atoms and ions in Hall thrusters Plasma Sources Sci. Technol. 28 105005
- [45] Chaplin V H, Johnson L K, Lobbia R B, Konopliv M F, Simka T and Wirz R E 2022 Insights from collisional-radiative models of neutral and singly ionized xenon in Hall thrusters J. Propul. Power 38 866
- [46] Priti, Gangwar R K and Srivastava R 2019 Collisional-radiative model of xenon plasma with calculated electron-impact fine-structure excitation cross-sections *Plasma Sources Sci. Technol.* 28 025003
- [47] Zhu X M and Pu Y K 2010 A simple collisional–radiative model for low-temperature argon discharges with pressure

- ranging from 1 Pa to atmospheric pressure: kinetics of Paschen 1s and 2p levels *J. Phys. D: Appl. Phys.* **43** 015204
- [48] Zhu X M, Cheng Z W, Pu Y K and Czarnetzki U 2016 Escape factors for Paschen 2p–1s emission lines in low-temperature Ar, Kr, and Xe plasmas J. Phys. D: Appl. Phys. 49 225204
- [49] Takahashi K, Charles C, Boswell R, Lieberman M A and Hatakeyama R 2010 Characterization of the temperature of free electrons diffusing from a magnetically expanding current-free double layer plasma J. Phys. D: Appl. Phys. 43 162001
- [50] Lieberman M A and Lichtenberg A J 2005 Principles of Plasma Discharges and Materials Processing (Wiley)
- [51] Meeker D 2023 Finite Element Method Magnetics (available at: www.femm.info/wiki/HomePage)
- [52] Boffard J B, Jung R O, Lin C C, Aneskavich L E and Wendt A E 2011 Optical diagnostics for characterization of electron energy distributions: argon inductively coupled plasmas *Plasma Sources Sci. Technol.* 20 055006
- [53] Ning Z X, Liu C G, Zhu X M, Wang Y F, An B J and Yu D R 2021 Diagnostic and modelling investigation on the ion acceleration and plasma throttling effects in a dualemitter hollow cathode micro-thruster Chin. J. Aeronaut. 34 85
- [54] Xia G J 2020 Research on krypton hall thruster with high specific impulse *PhD Thesis* Harbin Institute of Technology
- [55] Sartori E and Veltri P 2012 AVOCADO: a numerical code to calculate gas pressure distribution *Vaccum* **90** 88
- [56] Wang Y F, Zhu X M, Jia J W, Zhang Y H, Liu C G, Ning Z X and Yu D R 2023 Development of a circumferential-scanning tomography system for the measurement of 3D plume distribution of the spacecraft plasma thrusters *Measurement* 216 112966
- [57] Kim J, Lee D, Doh G, Park S, Kim H and Choe W 2022 Three-dimensional tomographically reconstructed optical emission profiles of Hall thruster plasmas *Plasma Sources Sci. Technol.* 31 015013
- [58] Dankongkakul B and Wirz R E 2017 Miniature ion thruster ring-cusp discharge performance and behavior *J. Appl. Phys.* **122** 243303

- [59] Dankongkakul B 2017 Overcoming the scaling limitations of ring-cusp DC ion thruster discharges *PhD Thesis* University of California
- [60] Yamashita Y, Tani Y, Tsukizaki R, Koda D and Nishiyama K 2019 Numerical investigation of plasma properties for the microwave discharge ion thruster μ10 using PIC-MCC simulation *Phys. Plasmas* 26 073510
- [61] Zhu X M, Pu Y K, Celik Y, Sarah S, Schüngel E, Luggenhölscher D and Czarnetzki U 2012 Possibilities of determining non-Maxwellian EEDFs from the OES line-ratios in low-pressure capacitive and inductive plasmas containing argon and krypton *Plasma Sources Sci. Technol.* 21 024003
- [62] Zhu X M and Pu Y K 2011 Determination of non-Maxwellian electron energy distributions in low-pressure plasmas by using the optical emission spectroscopy and a collisional-radiative model *Plasma Sci. Technol.* 13 267
- [63] Wachs B N and Jorns B A 2021 Optimization of an ECR thruster using single, two frequency, and pulsed waveforms AIAA Propulsion and Energy Forum On-line Conf. (9–11 August) (https://doi.org/10.2514/6.2021-3382)
- [64] Ji T Y, Wei L Q, Wang Y F, Song Y, Cai H K, Li H, Ding Y J and Yu D R 2022 Influence of pulse frequency on discharge characteristics of micro-cathode arc thruster *Vacuum* 196 110748
- [65] Gangwar R K, Dipti, Srivastava R and Stafford L 2016 Spectroscopic diagnostics of low-pressure inductively coupled Kr plasma using a collisional–radiative model with fully relativistic cross sections *Plasma Sources Sci. Technol.* 25 035025
- [66] Jung R O, Boffard J B, Anderson L W and Lin C C 2005 Electron-impact excitation cross sections from the xenon J = 2 metastable level *Phys. Rev.* A 72 022723
- [67] Boffard J B, Chiaro B, Weber T and Lin C C 2007 Electron-impact excitation of argon: optical emission cross sections in the range of 300–2500 nm *Atom. Data Nucl.* Data 93 831